Nucleic Acids Research, 2026, **54**, gkag544
https://doi.org/10.1093/nar/gkag544
Data Resources and Analyses

Single-base resolution atlas reveals moderate conservation and regulatory diversity of m^{6}A modifications across mammals

Xiaoxiao Zhang[1,2,†], Zhan Zhang[1,2,†], Weiqiang Liu[1,3,†], Wenfu Liu[1,2], Meng Li[1], Weixiao Chen[1,2], Gaoming Liu[1], Yichen Dai[4], Zihao Li[1,2], Chunyan Hu[1,2], Qi Pan[1,2], Yang Yu[5], Xiangye Liu[1,2], Pingfen Zhu[1], Xuming Zhou[1,*]

[1]State Key Laboratory of Animal Biodiversity Conservation and Integrated Pest Management, Institute of Zoology, Chinese Academy of Sciences, Beijing 100101, China
[2]University of Chinese Academy of Sciences, Beijing 100049, China
[3]Department of Neurology at Yale School of Medicine, Yale University, New Haven, CT 06510, United States
[4]School of Life Sciences, Fudan University, Shanghai 200438, China
[5]School of Life Sciences, University of Science and Technology of China, Anhui 230026, China

*To whom correspondence should be addressed. Email: zhouxuming@ioz.ac.cn
†These authors contributed equally to this work.

Abstract

RNA methylation, notably m^{6}A modification, is a predominant epitranscriptomic alteration in mRNA, yet its evolutionary properties and the selective constraints acting on it across mammals remain poorly understood. Here, we generated a single-base-resolution m^{6}A modification atlas in liver, kidney, and brain tissues across 21 non-model mammals using Nanopore direct RNA sequencing. We found that 25.54–35.70% of orthologous transcripts across examined species harbor m^{6}A modifications, with m^{6}A-modified sites exhibiting significantly greater conservation than nearby unmodified regions, probably under purifying selection. While m^{6}A sites were preferentially enriched in RNA loops rather than stems, an inverse correlation between overall m^{6}A levels and RNA splicing complexity was observed, a pattern which is compatible with a model in which exon junction complex (EJC)-associated, splice-junction-proximal mechanisms contribute to suppression of nearby m^{6}A deposition. Further analyses of m^{6}A-modified genes and life history traits uncovered that genes with higher m^{6}A modification ratios in long-lived mammals were mainly characterized by relaxed selection. This study explores the evolutionary landscape of m^{6}A modifications in non-model organisms, underscoring their diverse regulatory roles and evolutionary significance across mammalian lineages.

Graphical abstract

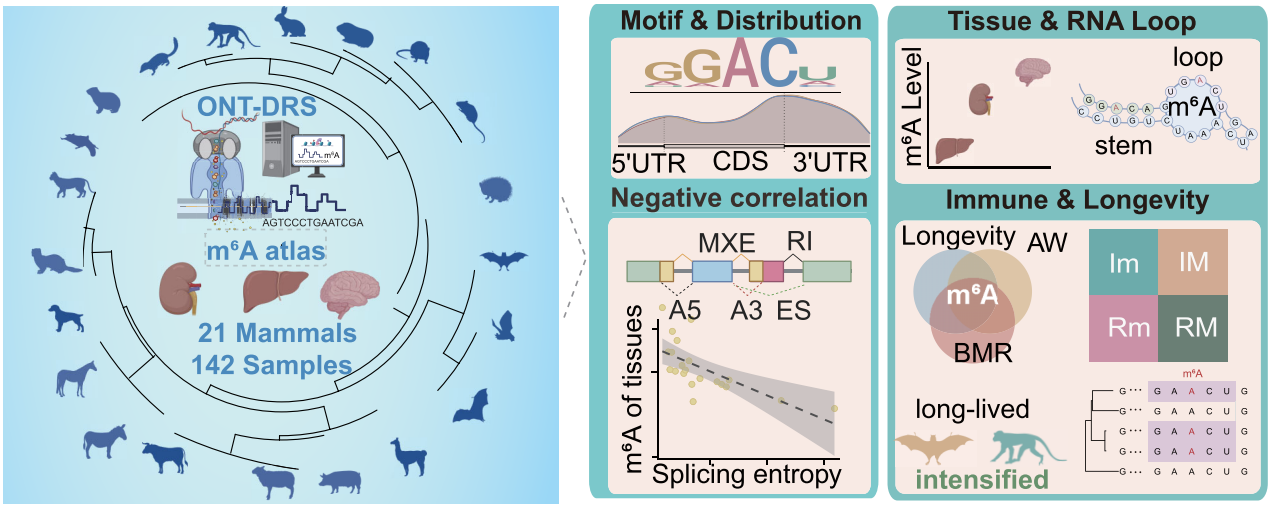

Received: November 8, 2025. **Revised:** March 29, 2026. **Accepted:** May 7, 2026

Introduction

RNA methylation modifications, a novel avenue of epitranscriptomic regulation, have garnered extensive research attention. Currently, ∼180 distinct chemical modifications have been identified within RNA nucleotide residues [1, 2], spanning all types of RNA molecules, including tRNA, rRNA, mRNA, as well as various short and long non-coding RNAs (lncRNAs) [3–8]. Although the presence and abundance of m^1A [9] and ac^4C [10] on mRNA remain under investigation, a variety of chemical modifications have been reported on mRNA (m^6A, m^7G, m^5C, hm^5C, Ψ, etc.), among which N^6-methyladenosine (m^6A) stands out as the most prevalent and abundant chemical modification in eukaryotic mRNA. The m^6A modification process is orchestrated by crucial proteins commonly referred to as "writers", "readers", and "erasers", which respectively add, recognize, and remove the m^6A chemical modification from RNA bases [11–14]. The significance of m^6A modification extends beyond its prevalence, as it has been implicated in various diseases such as obesity, infertility, cancer, heart failure, autoimmune disorders, and neuromuscular defects [15–19]. Additionally, it is intricately involved in a diverse array of biological processes, including viral infections, stress responses, heat shock, and DNA damage, and also governs crucial molecular functions, such as RNA–protein interactions, RNA structure, stability, dynamics, alternative splicing, polyadenylation, transport, localization, and translation efficiency [12, 20–28]. This wealth of evidence emphasizes the multifaceted impact of m^6A modification on RNA biology, encouraging further exploration and understanding of its intricate regulatory mechanisms and potential therapeutic implications.

Although m^6A modifications across different tissues within the same species have been extensively studied [29], cross-species comparisons have predominantly focused on model organisms such as mice, rats, and humans [30–32]. Consequently, the exploration of m^6A modifications in non-model organisms remains significantly underdeveloped. Third-generation sequencing technologies, such as Oxford Nanopore Technologies' direct RNA sequencing (ONT-DRS) and PacBio sequencing, have broadened the field of epitranscriptomics, by eliminating amplification biases, offering single-molecule sensitivity, and enabling quantitative assessment of modification levels [33–35]. Furthermore, these methods allow for cross-species and cross-tissue sample comparisons, facilitating absolute transcript quantification and accurate structural identification. Here, we generated and analyzed the m^6A modification atlas across 21 mammalian species using Nanopore DRS combined with a benchmarked m6Anet detection framework (Fig. 1A). Our findings demonstrate that m^6A modification exhibits a moderate level of conservation across species, underscoring its evolutionary significance. Furthermore, our results indicate that RNA m^6A methylation may influence the splicing process and reveal a significant correlation between splice complexity and methylation patterns. These insights advance our understanding of RNA modifications and offer new perspectives on the role of epitranscriptomics in species evolution and biodiversity.

Materials and methods

Animal samples

All animal care and experimental protocols of this study were approved by the Institute of Zoology, Chinese Academy of Sciences (no. IOZ-IACUC-2022-216) and were in accordance with institutional animal welfare guidelines. To elucidate the intricate landscape of m^6A modifications in mammalian species, we conducted a comprehensive analysis involving 142 tissue samples from liver, kidney, and brain. These samples represented 21 mammalian species across 11 orders (Supplementary Tables S1 and S2), with intra-lineage evolutionary distances ranging from 11 to 62 million years and inter-lineage distances extending from 74 to 160 million years. Our selection aimed to represent a broad spectrum of orders across major taxonomic levels. We included a diverse array of economically significant and domesticated species, alongside several understudied and phenotypically distinct mammals such as bats, tree shrews, sugar gliders, and four-toed hedgehogs. The selection criteria for both species and tissues were healthy, adult to middle-aged male individuals, and each tissue comprising 1–3 biological replicates.

Sample collection and RNA preparation

Species were categorized based on their longevity, while collecting relevant information such as body weight and basal metabolic rate. To account for variations in tissue structure and cellular composition across different species, we conducted organ homogenization on the major portions of the organs in advance. Approximately 100 mg of homogenized tissue was then extracted for subsequent RNA isolation. In the case of brain tissue, a distinctive methodology was implemented. Specifically, samples were collected from the forebrain, ensuring a specific focus on this particular region. For species with limited brain sizes, brain regions other than the olfactory bulb and cerebellum were targeted to ensure comprehensive coverage. Immediately after collection, the samples were immersed in RNA-later preservation solution and left to penetrate fully at 4°C overnight before being transferred to a −80°C freezer for long-term storage. To ensure comparability of samples from homologous organs across species, all samples underwent grinding in liquid nitrogen within the research laboratory for RNA extraction.

Total RNA of each sample was extracted in accordance with the standard protocol of the Total RNA Kit I (R6834 Total RNA Kit I). Each sample contained 20 μg of total RNA for DRS. RNA was cleaned and concentrated by the NEBNext® Poly (A) mRNA Magnetic Isolation Module (E7490S) according to the manufacturer's instructions. From each sample, 1 μg of total RNA was prepared for the RNA integrity and concentration measurement using NanoDrop (Thermo Fisher Scientific).

Construction of the Nanopore sequencing library and sequencing

The prepared RNA of each sample was utilized for preparation of a DRS library using the Oxford Nanopore DRS protocol (SQK-RNA002, Oxford Nanopore Technologies). For reversed connector connection, 9 μl of prepared RNA, 3 μl of NEBNext® Quick Ligation Reaction Buffer (NEB), 1 μl of RT Adapter (RTA) (SQK-RNA002), and 2 μl of T4 DNA ligase (NEB) were mixed together and incubated under 25°C for 10 min. Afterwards, 8 μl of 5× first-strand buffer (NEB), 2 μl of 10 mM dNTPs (NEB), 9 μl of nuclease-free water, 4 μl of 0.1 M dithiothreitol (DTT; Thermo Fisher), and 2 μl of SuperScript™ III Reverse Transcriptase (Thermo Fisher Scientific, Catalog number: 18 080 044) were added into the above 15 μl reaction system and incubated under 50°C for 50 min then 70°C for 10 min. Reverse-transcribed mRNA was puri-

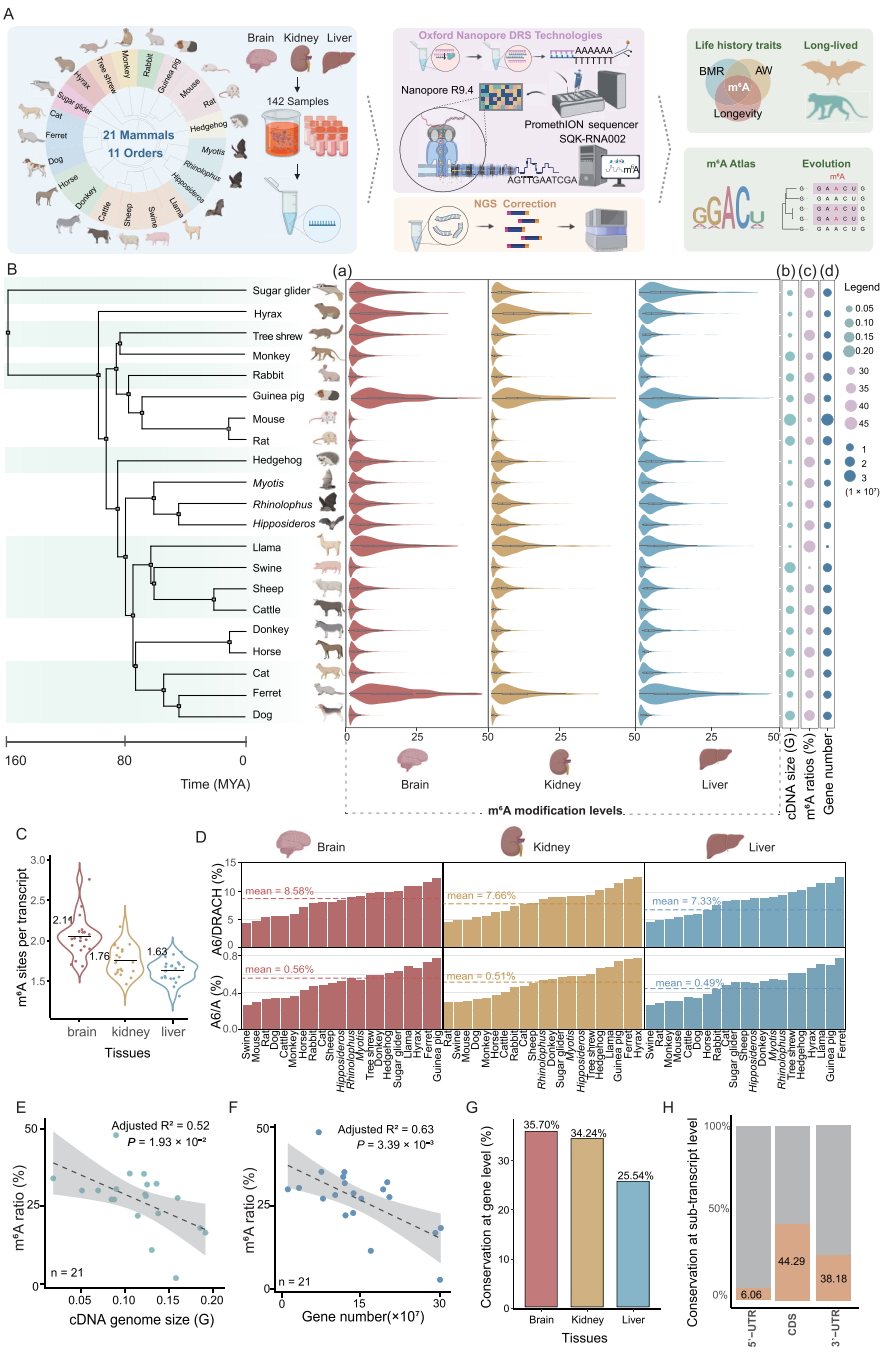

Figure 1. Comparative profiles and evolutionary characters of m^{6}A RNA modifications across 21 mammals. (**A**) Overview of sampling, RNA sequencing, and data analysis conducted on brain, kidney, and liver tissues of 21 mammalian species. RNA sequencing utilized the Oxford Nanopore PromethION platform and was corrected with next-generation sequencing data. Key analyses included m^{6}A methylation patterns, transcript expression, alternative splicing, evolutionary conservation of m^{6}A sites, and correlations with life history traits. (**B**) Mammalian phylogeny, with violin plots depicting m^{6}A modification levels across tissues, and box plots illustrating M_{Gene} distribution. (a) Each violin plot encompasses the m^{6}A modification levels of all genes within a tissue. The boxplot represents the distribution of M_{Gene} values. The central horizontal line within the box indicates the median value. The upper and lower edges of the box represent the first (Q1) and third quartiles (Q3), respectively, showing the interquartile range (IQR). The whiskers extend to the smallest and largest values within 1.5 times the IQR from Q1 and Q3, respectively. (b) Bubble plot representing the total cDNA size in gigabases (G) mapped for each species. (c) Bubble plot illustrating the global m^{6}A modification ratios (%) across the transcriptomes of the respective species. (d) Bubble plot indicating the total number of genes detected. The size and color intensity of the bubbles in panels b, c, and d correspond to the numerical ranges provided in the rightmost key. Species name annotation: *Myotis* (*Myotis chinensis*), *Rhinolophus* (*Rhinolophus pusillus*), *Hipposideros* (*Hipposideros larvatus*). (**C**) Frequency distribution of m^{6}A sites per transcript across three tissues. (**D**) Proportions of m^{6}A sites conforming to DRACH motifs compared with total adenines. (**E** and **F**) The *y*-axis represents the m^{6}A modification level of a tissue. DRACH reads refer to the sum of all reads at DRACH motif sites in the sample. Correlation analyses of m^{6}A modification levels with cDNA genome size and gene number, using a phylogenetic regression approach. The most appropriate model selected is the Ornstein–Uhlenbeck model. The m^{6}A methylation levels show a significant negative correlation with gene number in liver. Similarly, m^{6}A methylation levels are significantly negatively correlated with cDNA genome size in liver. (**G** and **H**) Conservation patterns of m^{6}A modifications in orthologous genes across multiple species and their distribution across transcript regions (5′-UTR, CDS, and 3′-UTR).

fied with 1.8× Agencourt RNAClean XP beads and washed with 23 μl of nuclease-free water, and subsequently sequencing adapters were added using 8 μl of NEBNext Quick Ligation Reaction Buffer (New England Biolabs, NEB), 6 μl of RNA adapter (RMX), and 3 μl of T4 DNA ligase. The mix was purified and washed again as above, and 75 μl of RNA running buffer (RRB; SQK-RNA002) were added with 35 μl of nuclease-free water. This final reaction system was loaded into the Nanopore R9.4.1 sequencing micro-array and sequenced for 48–72 h using the PromethION sequencer (Oxford Nanopore Technologies).

Processing, alignments, and analysis of novel genes and transcripts

To assess the read quality, raw reads were called using Guppy [36] (version: 5.0.16 + b9fcd7b) base-calling software (Oxford Nanopore, Oxford, UK), and adapter sequences were also trimmed by Guppy. Guppy was only available to ONT customers via their community site (https://community.nanoporetech.com). Low quality reads (Q-value < 7) and short-length reads (< 50 bp) were filtered by Nanofilt (version: 2.8.0) [37]. The remaining clean reads were corrected using the fmlrc2 (version: 0.1.4) with our short-length RNA-seq data [38]. Afterwards, clean reads from each library were aligned to the reference genomes from 21 species. Specific reference genome versions and sources are called using Minimap2 (version: 2.17, parameters: -r 941) [39]. The alignment ratios were calculated using Samtools (version: 1.11) [40]. To reduce the redundancy of the alignment, we merge the alignment with only differences in exons at the 5′ end, and obtain the non-redundant transcript sequence using StringTie [41] (version: 2.1.4, parameters: -conservative -L -R). Gffcompare [42] (version: 0.12.1, parameters: -R -C -K -M) was used to compare the transcripts with the known transcripts of the genome and find new transcripts and new genes.

Sequencing, assembly, and annotation of the four-toed hedgehog and the sugar glider genome

The genomic DNA was extracted from the muscle tissue of sugar glider (*Petaurus breviceps*) and the four-toed hedgehog (*Atelerix albiventris*) samples. The tissues were obtained from euthanized individuals and ground in liquid nitrogen before being transferred to the laboratory. A 2.0 ml EP tube was prepared by adding 1.0 ml of nuclear lysis buffer, 100 μl of proteinase K (20 mg ml^{-1}), and 100 μl of sodium dodecylsulfate (SDS; 20%), and pre-heated to 56°C. Approximately 50–100 mg of tissue was collected using a scalpel blade, added to the pre-heated EP tube, and either minced or ground. The samples were incubated at 56°C for 1–2 h and centrifuged at 12 000 × g at room temperature for 10 min. The supernatant was transferred to a new 2.0 ml EP tube, mixed with an equal volume of phenol/chloroform/isoamyl alcohol (25:24:1), and vigorously inverted. After centrifugation at 12 000 × g at room temperature for 10 min, the supernatant was transferred to a new 1.5 ml centrifuge tube, avoiding the intermediate protein layer. Two-thirds of the supernatant volume of isopropanol and 100 μl of sodium acetate were added, gently mixed by inversion, and the mixture was stored at −20°C for at least 2 h to allow DNA precipitation. The precipitate was centrifuged at 18 213 × g at room temperature for 15 min, and the supernatant was discarded. The pellet was washed with 1 ml of 75% ethanol, pipetted gently to resuspend, and centrifuged at 18 213 × g at room temperature for 3 min. After removing the supernatant, any residual liquid was removed by a brief centrifugation, and the pellet was air-dried for 3–5 min. Finally, 20–200 μl of TE buffer was added to dissolve the DNA pellet [43].

The genomic DNA was used to construct the single-tube Long Fragment Read (stLFR) library using the MGI Easy stLFR Library Prep Kit* (MGI, Shenzhen, China) following the manufacturer's protocol [44]. Transposons were used to insert a hybridization sequence every 200–1000 bp on genomic DNA molecules. Then the transposon-integrated DNA was mixed with beads. Each bead contained 400 000 copies of an adapter sequence which involved a unique barcode shared by all adapters on the bead, a common PCR primer site, and a common capture sequence complementary to the sequence on the integrated transposons. After capturing the genomic DNA on the beads, the transposons were ligated to the barcode adapters. PCR was performed after the ligation step. The stLFR library was sequenced on BGISEQ-500 and DNBSEQ-T1 platforms. We also constructed Hi-C libraries from four-toed hedgehog and sugar glider to anchor scaffolds onto the chromosome. In brief, freshly cut muscle tissues were vacuum infiltrated in nuclei isolation buffer supplemented with 2% formaldehyde. The addition of glycine and additional vacuum infiltration stopped cross-linking. Fixed tissue was ground to powder before being resuspended in nuclei isolation buffer to obtain a suspension of nuclei. Purified nuclei were digested with MboI restriction enzyme and stained by biotin-14-dATP. T4 DNA polymerase removed biotin-14-dATP from non-ligated DNA ends. The ligated DNA was sheared into 300–600 bp fragments, blunt-end repaired and A-tailed, and purified using biotin–streptavidin-mediated pull-down. The Hi-C libraries were then sequenced on the BGISEQ-500 and DNBSEQ-T1 platform.

We implemented Supernova v2.1.1 [45] to acquire initial genome assembly after filtration for the removal of barcode sequences, adapters, and reads with low quality using SOAPfilter v2.2 [46]. Reads with > 10% low-quality bases (Q < 10) were discarded. Adapter contamination and PCR duplication reads were also filtered. The initial assembly was generated under "pseudohap" style in Supernova. Gaps between contigs within the same scaffolds were filled by Gapcloser software, and purge haplotigs v1.1.1 [47] was employed to remove the redundant sequences. We achieved 2.57 and 3.38 Gb draft assemblies with 0.13 and 0.50 Mb scaffold N50, and 0.019 and 0.029 Mb contig N50 of four-toed hedgehog and sugar glider, respectively. We also generated a Hi-C library for chromosome anchoring of sugar glider and four-toed hedgehog with MboI restriction enzyme. Hi-C clean reads were pre-processed using HiC-Pro v2.8.0 [44] to obtain valid pairs of reads involving two different restriction fragments. Those valid read pairs were aligned to the genome draft using the Juicer v1.5 [48] pipeline with removal of duplicates and near duplicates to establish Hi-C contact matrixes. With the assistance of close species karyotype for clustering, we anchored draft scaffolds to form pseudochromosomes according to Hi-C contact matrixes using a 3D *de novo* assembly (3d-dna, v170123) [49] pipeline. We visualized the contact density map in Juicebox v1.11.08 [50] for manually polishing scaffolding faults. Finally, 87.29% and 93.71%, respectively, of four-toed hedgehog and sugar glider scaffold lengths were anchored to 22 and 11 chromosomes, and an improved scaffold N50 of 106.05 and 363.52 Mb was achieved.

We used RepeatMasker v4.1.5 (www.repeatmasker.org/) for homology-based repeat annotation with ther Repbase library (version 20 181 026) and RepeatModeler v2.0.1 software for *de novo* repeat annotation [51]. RepeatClassifier embedded in RepeatModeler and TEclass v2.1.3 [52] were utilized to predict transposon elements. Repeat ProteinMask v4.0.9 [53] and Tandem Repeat Finder v4.10.0 [54] were employed to annotate repeat proteins and tandem repeats, respectively. After hard-masking, we used Augustus v3.1.0 [55] and Genscan v1.0 [56] to predict gene models using human genes as the training set. Homology annotations were predicted with genes from human and sibling species including *Erinaceus europaeus*, *Condylura cristata*, *Suncus etruscus*, *Galemys pyrenaicus*, *Sorex araneus*, and *Homo sapiens* for four-toe hedgehog, and *Trichosurus vulpecula*, *Vombatus ursinus*, *Phascolarctos cinereus*, *Dromiciops gliroides*, *Sarcophilus harrisii*, and *H. sapiens* for sugar glider. We searched for peptide sequences (BLAT v36 [57]) and predicted the coding sequence (GeneWise v2.4.1 [58]). ONT-DRS transcripts were used for identifying open reading frames with TransDecoder v5.5.0 [59]. The aforementioned *ab initio* prediction, homology, and transcript annotation were integrated by Glean to generate final protein-coding gene sets including 30 587 and 29 642 genes of four-toe hedgehog and sugar glider, respectively. rRNA and tRNA were identified using BLASTN with human rRNA and tRNAscan-SE v1.3.1 [60], respectively. We used INFERNAL v1.1.1 [61] software to annotate small nuclear RNA (snRNA) and microRNA (miRNA) against the Rfam v14.1 database [62].

Preparation and sequencing of MeRIP libraries

Following the manufacturer's protocol, total RNA was immunoprecipitated using the m^{6}A-IP Kit (GenSeq Inc.). Briefly, RNA was fragmented into ∼200 nt using the RNA Fragmentation Reagent, and Protein A/G beads were prepared by rotating them for 1 h to bind the antibody. The bead–antibody complexes were then incubated with the fragmented RNA at 4°C for 4 h. After incubation, the RNA–antibody complexes were washed multiple times. Subsequently, the bound RNA was eluted and purified. RNA libraries for both immunoprecipitated and input samples were prepared using the Low Input Whole RNA Library Prep Kit (GenSeq) according to the manufacturer's instructions. The quality of the libraries was assessed using an Agilent 2100 Bioanalyzer, and high-throughput sequencing was performed on an Illumina NovaSeq X Plus platform in paired-end mode [33].

Correlation between gene expression level and modification level

The expression level of a gene refers to the mean counts per million (CPM).

$$\mathrm{CPM} = \frac{\text{direct RNA counts of a gene}}{\text{all mapped reads of a sample} \times 10^6}$$

When conducting the correlation analysis between the gene expression level and the modification level of species, we calculated the correlations separately according to the tissues, namely liver, kidney, and brain. The correlation analysis was carried out at both the gene level and the species level. The modification level of a gene is represented by M_{Gene}, and the expression level of a gene is represented by CPM. The modification level of a species refers to the median value of M_{Gene} in one of the liver, kidney, and brain tissues of that species, while the gene expression level of a species is the median value of the CPM of all genes in this sample. Phylogenetic influence was accounted for by using the phytools R package [63] in the correlation analysis.

Identification and estimation of m^{6}A RNA methylation

To identify m^{6}A modification sites, we used Nanopolish (version 0.14.0) [64] and m6Anet (version: 2.0.2) [65] with the pre-trained HCT116_RNA002 model. During the detection process, m6Anet randomly sampled at least 20 reads from each site and calculated the average probability of modification through multiple rounds of sampling. The number of sampling iterations was controlled by the –num_iterations parameter, with a default value of 5, which balances stability and reduced runtime. M6Anet calculated the modification probability for each candidate site, and the mod_ratio represents the proportion of modified reads at a specific site relative to the total reads. To enhance reliability, we conducted a systematic evaluation of detection thresholds and their impact on m^{6}A site identification. Our analysis revealed a clear precision– recall trade-off: increasing the probability threshold substantially improved accuracy—as measured by overlap with m^{6}A-seq peaks—but resulted in fewer identified sites (Supplementary Figs S43 and S44). To ensure accuracy, we applied a stringent threshold, selecting sites with a modification probability > 0.9 as reliable m^{6}A modification sites.

We defined several metrics to measure m^{6}A modification levels at the tissue, motif, site, and gene levels. For tissues, the modification level M_{tissue} is calculated as the proportion of m^{6}A-modified reads to the total reads of sites conforming to the DRACH motif within a tissue. In the numerator, the sum of reads supporting each m^{6}A site is used. For example, if a single read contains two m^{6}A sites, it is counted twice. Similarly, in the denominator, all reads associated with the DRACH motif are counted. If a read contains two DRACH motifs, it is also counted twice, regardless of whether the motifs are modified as DRA^{6}CH. This definition accounts for gene expression levels, the number of adenines (A) (reflecting gene length), and the sample's library size (Supplementary Figs S45–S47; Supplementary Table S38).

$$M_{tissue} = \frac{\text{sum of m}^6\text{A reads of a site in a tissue}}{\text{all DRACH reads of a site in the library}}$$

For the modification level of a gene, M_{Gene} is defined as the total number of m^{6}A-modified reads in the gene divided by the total number of reads for the gene, further divided by the total number of DRACH motif reads (i.e. the library size) in the sample.

$$M_{Gene} = \frac{\text{sum ofm}^6\text{A reads of a site in a gene}}{\text{all reads of a site in a gene}} \Big/ \text{all reads of DRACH in the library} \times 10^9$$

The modification level of a specific motif type, M_{motif}, is defined as the total number of reads for a particular modified motif type in the sample divided by the total number of reads matching that motif type in the sample, further divided by the

total number of DRACH motif reads in the sample.

$$M_{motif} = \frac{\text{The reads of each DRA}^6\text{CH site within a tissue}}{\text{The reads of this DRACH type site within a tissue}} \text{/all reads of DRACH in the library} \times 10^9$$

The m^{6}A modification level of a specific site, M_{site}, is defined as the number of reads at that site divided by the total number of reads for the gene containing the site, further divided by the total number of DRACH motif reads in the sample.

$$M_{site} = \frac{\text{m}^6\text{A reads of a site}}{\text{all reads of a site in a gene}} \text{/all reads of DRACH in the library} \times 10^9$$

Although our m^{6}A atlas was generated using Nanopore RNA002 chemistry, we ensured high data fidelity by implementing a rigorous hybrid correction pipeline with short-read sequencing to achieve > 99% sequence identity, coupled with stringent probability filtering (score > 0.9) using the m6Anet algorithm. To comprehensively benchmark this pipeline, we validated the dataset against multiple orthogonal methodologies. First, the m6Anet model inherently minimizes false-positive background noise by incorporating modification-free *in vitro* transcribed (IVT) RNA during its development. For quantitative accuracy, our predicted modification probabilities showed strong concordance with chemical-based absolute quantification, demonstrating a highly significant positive correlation with GLORI-seq measurements in HEK293 cells across 3219 shared loci (Pearson $r = 0.67$, $P < 0.0001$; Supplementary Fig. S48), as well as consistency with colorimetric assays (Supplementary Figs S9 and S10; Supplementary Table S28). Furthermore, positional validation against newly generated and publicly available MeRIP-seq data across corresponding species exhibited robust spatial agreement, with a median overlap of 85.57% (Supplementary Fig. S5). Together, these rigorous controls and orthogonal validations confirm that our analytical framework effectively captures bona fide m^{6}A modifications, providing a highly reliable basis for cross-species evolutionary analyses.

Identification of OGs and SGs among 21 species

The protein sequences of 428 816 protein-coding genes from 21 species were used to construct orthogroups using OrthoFinder (version: 2.4.0) [66] with default parameters. Briefly, (i) only the longest protein was selected for identification when several isoforms were available for one gene, (ii) DIAMOND (version: 0.9.24) [67] was used to obtain similarity relationship between protein sequences, and (iii) the MCL graph clustering algorithm was used to cluster genes into orthogroups. In total, 21 609 orthogroups were identified. To better categorize the genes, we assigned the designation of 'OGs' (orthogroup genes) to those that appeared in non-species-specific orthogroups and were present in at least two species. Genes that did not fulfill these criteria were classified as 'SGs' (species-specific genes).

Sequence alignment and evolutionary selection analysis

For each set of orthologous genes, multiple sequence alignments were performed using MAFFT (version: 7.310) with default parameters [68]. To ensure the inclusion of only conserved regions, the alignments were subjected to conservative filtering using GBlocks (version: 0.91b) [69]. The sequences obtained from the analysis preserved at least 75% of conserved sites, and the shortest flanking sequences exceeded 85% of the aligned length, ensuring the retention of crucial information. To reduce false positives in subsequent evolutionary selection analysis, regions with more than three consecutive non-conserved sites were considered to have lower alignment quality and were removed. Additionally, sites with missing data in over half of the species were also eliminated to ensure robustness. During filtering, a block size of 5 was used. Moreover, to further mitigate the risk of false positives, genes with < 10 representative species were excluded from the analysis.

The phylogenetic relationships for all mammalian species were obtained from the TIMETREE database [70]. To estimate selection pressures, the FUBAR site model in the HYPHY software was used to test different categories of mammals, ultimately providing information on the selection pressure ($\alpha < \beta$ and $\alpha > \beta$) for each gene. To assess the strength of relaxed selection on each branch and gene, the RELAX model in HYPHY [71] was used to compute the relaxation coefficient ($\omega_{\text{background branch}}{}^{k} = \omega_{\text{foreground branch}}$) between foreground and background branches. A selection intensity parameter $k > 1$ indicated intensified positive selection, while $k < 1$ indicated relaxed selection. All parameter estimates obtained were utilized in subsequent analyses. Conservation scores for each site were calculated using GERP++ (gerpelem) [72] and Rate4Site (version: 3.0.0) [73].

Codon-position-matched controls in coding sequences

To control for coding-related confounders, we performed a codon-position-matched conservation analysis in coding sequences (CDSs) using per-site m^{6}A call tables with mapped human genomic coordinates (chr, 1-based position), region annotation, and phastCons scores. Because human transcript identifiers were not available, each CDS site was assigned to an inferred protein-coding human transcript using the GRCh38 GTF annotation by selecting, among all protein-coding transcripts whose CDS overlaps the site, the transcript with the longest total CDS length to obtain a reproducible reading frame. We computed each site's CDS coordinate by traversing merged CDS exons according to transcript strand and defined codon position as codon_pos = [(CDS_pos - 1)mod3] + 1. For each CDS m^{6}A site, we selected one nearby unmodified control adenine within a ± 200 nt window that was not in the m^{6}A site set, lay within the CDS of the same inferred transcript, matched the same codon position (1/2/3), and was an "A" in the GRCh38 reference genome; candidates overlapping the 3′-untranslated sequence (UTR) were excluded (the UTR was prioritized when overlap occurred), and the nearest eligible candidate was chosen when multiple candidates existed. PhastCons scores for controls were retrieved from per-chromosome phastCons tracks, and differences between m^{6}A sites and matched controls were tested using two-sided Wilcoxon rank-sum tests stratified by codon position (1/2/3) and visualized with violin/box plots with mean and median annotations.

Restriction to 4-fold degenerate sites

To minimize potential amino acid level confounding in CDSs, we performed an additional analysis restricted to 4-fold de-

generate (4D) sites. Using the inferred transcript frame and the GRCh38 reference sequence, we reconstructed the codon for each CDS site and classified a site as 4D if it occurred at codon position 3 and if substituting the third base with A/C/G/T did not change the encoded amino acid under the standard genetic code (excluding stop codons and codons containing ambiguous bases). We then restricted both the CDS m^{6}A and matched control sets to 4D sites and compared phastCons distributions using a two-sided Wilcoxon rank-sum test, with visualization analogous to the codon-position-stratified analysis.

Phylogenomic stratigraphy

We employed the phylogenomic stratigraphy method [74] to trace the evolutionary origins of m^{6}A-modified genes in mammals. Expanding from the original 21 mammalian species, we included nine additional representative species: *H. sapiens*, *Saccharomyces cerevisiae*, *Caenorhabditis elegans*, *Ciona intestinalis*, *Petromyzon marinus*, *Danio rerio*, *Xenopus tropicalis*, *Cyanistes caeruleus*, and *Ornithorhynchus anatinus*. The phylogenetic tree was temporally calibrated using divergence times from TimeTree [75] and divided into nine phylostratigraphic layers based on their evolutionary chronology. Using *H. sapiens* as the focal species, the phylostratr software [76] was applied to trace the earliest emergence layers of human genes. Additionally, we mapped the origins of m^{6}A-modified orthologous genes shared between humans and 21 mammals across liver, kidney, and brain tissues, quantifying their abundance and modification levels within each phylostratigraphic layer.

Tissue specificity analysis

To identify genes with tissue-specific modifications, the tissue-specific expression index (tau, τ) was calculated for the modification level of each gene in different tissues to characterize the specificity of gene modification [77]. The specific formula is as follows:

$$\text{tau} = \frac{\sum_{i=1}^{n} 1 - \hat{x}_i}{n-1}; \hat{x}_i = \frac{x_i}{\max\limits_{1 \le i \le n} x_i}$$

where x_i is the average modified ratio of m^{6}A sites in a tissue, and n is the number of tissues being studied.

Structural analysis of gene transcripts

Suppa2 [78] was used to obtain alternative splicing events for each sample, and Suppa2 diffSplice [79] was used to identify the difference variable splice between groups. We quantified entropy-based splicing complexity for each alternative splicing event using splicing entropy (Shannon entropy), which captures the diversity/heterogeneity of isoform (pathway) usage within an event rather than the abundance of a specific alternative splicing event type. The calculation formula is as follows [80]:

$$\text{Splicing entropy} = -\sum_i \psi_i \log_2 \psi_i$$

Where ψ_i represents the relative expression level of the ith alternative splicing pathway of a transcription event ($0 \le \psi_i \le 1$). As can be seen from the above formula, the entropy value (splicing entropy), which measures alternative splicing complexity, refers to the heterogeneity (degree of inconsistency) of the relative expression of all splicing patterns. After dividing the resulting entropy values into different types (splicing entropy = 0 and > 0), the events of different complexity in each tissue of each species are counted.

For the positional analysis of m^{6}A sites relative to alternative splicing architectures, we utilized high-confidence m^{6}A sites with a modification probability threshold strictly > 0.9. Alternative splicing events, including skipped exons, mutually exclusive exons, alternative 5′ and 3′ splice sites, alternative first and last exons, and retained introns, were annotated using SUPPA. To construct the meta-event profiles, the genomic coordinates of these events were mapped onto a standardized meta-coordinate system consisting of an upstream flank, the event body, and a downstream flank. The flanking regions were set to a fixed length of 200 nucleotides. To accurately delineate the variable regions for alternative 3′ and 5′ splice site events and completely exclude intronic sequences, the event body was defined by the genomic difference between the competing splice coordinates. All positional mappings were performed in a strand-specific manner to preserve the 5′ to 3′ RNA directionality. Density profiles were generated using Gaussian kernel density estimation. When aggregating data across multiple species or biological replicates, a reciprocal weighting strategy was applied to ensure equal contribution from each dataset, preventing domination by samples with higher sequencing depths or site counts.

To quantitatively evaluate m^{6}A enrichment near splice boundaries, we defined analysis windows of 25, 50, and 100 nt located strictly upstream of the relevant alternative splicing junctions, based on the transcript strand direction. To rigorously control for local sequence context, base composition, and basal transcript abundance, we implemented a local upstream-shifted background strategy. For each splice-proximal window, a length-matched local background window was generated by shifting the coordinate exactly 200 nt further upstream along the same transcript. This shift distance was selected to ensure the background region was placed outside the anticipated physical footprint of the exon junction complex (EJC). Genomic sequences for these windows were extracted using the reference genome FASTA files. The raw m^{6}A modification ratio for each window was calculated by dividing the absolute number of high-confidence m^{6}A sites within the window by either the total number of adenosines or the total occurrences of the canonical DRACH sequence motif within that exact sequence.

For the exon-level classification and m^{6}A frequency analysis, all transcript exons were extracted from the reference GTF annotation. Exons were classified into constitutive or specific alternative categories based on their genomic overlap with the alternative splicing intervals defined by SUPPA. An exon was designated as m^{6}A modified if its genomic coordinates overlapped with at least one high-confidence m^{6}A site possessing a modification probability > 0.9. The modification fraction for each specific exon class was subsequently calculated as the number of m^{6}A-positive exons divided by the total number of identified exons within that category. Comparisons between constitutive and alternative exon classes were then conducted to evaluate the spatial distribution preferences of m^{6}A deposition at the exon level.

Regression analysis of m^{6}A modification levels and life history traits

To investigate the correlation between m^{6}A modification levels and life history traits while accounting for phylogenetic relationships, we employed phylogenetic generalized least squares (PGLS) regression. The analysis was conducted using both the Brownian motion (BM) model and the Ornstein–Uhlenbeck (OU) model to assess the evolutionary processes influencing trait variation. The phylogenetic tree used for PGLS was constructed based on available species relationships, and branch lengths were estimated accordingly. Model selection was performed by comparing the Akaike information criterion (AIC) values, with the best-fitting model used for subsequent analyses. The PGLS analysis was implemented in the R package caper [81], where m^{6}A modification levels were set as the dependent variable, and life history traits (e.g. longevity, adult body weight, and basal metabolic rate) as independent variables. Statistical significance was evaluated based on regression coefficients and *P*-value, providing insights into the evolutionary association between m^{6}A modifications and life history traits.

RNA secondary structure prediction

The locations of m^{6}A sites obtained from m6Anet [65] were utilized to extract fasta sequences containing m^{6}A sites from the reference genome. Subsequently, RNAfold [82] was employed for predicting the secondary structure of RNA. Python scripts were used to compile information from the obtained secondary structure results. The positions of m^{6}A sites were aligned with the sequence positions in the secondary structure prediction files to assess the secondary structure and quantity of both m^{6}A and non-m^{6}A sites. The positions of m^{6}A sites on each transcript were obtained from m6Anet. The transcript positions were then mapped to the corresponding genomic positions, and subsequently converted into a bed file representing the m^{6}A site distribution on the genome. Visualization of the m^{6}A site distribution in the liver, kidney, and brain of the same species was achieved using Guitar [83] (R version 4.3).

3-Deazaadenosine treatment for cell m^{6}A inhibition

The broad-spectrum inhibitor 3-deazaadenosine (3-DAA), which blocks the conversion of *S*-adenosylhomocysteine (SAH) to *S*-adenosylmethionine (SAM) by inhibiting SAH hydrolysis, was used for treatment. Primary fibroblast cells were isolated from the kidneys of horses, monkeys, and hyraxes, and cultured under standard conditions. Once proper cell attachment was confirmed, the cells were treated with 100 μM 3-DAA for 48 h to reduce global m^{6}A modification levels. After treatment, total RNA was extracted using a standard phenol–chloroform method, and m^{6}A modification levels were quantified using the EpiQuik m^{6}A RNA Methylation Quantification Kit (Colorimetric), following the manufacturer's protocol. Additionally, we must acknowledge that while the broad-spectrum inhibitor 3-DAA effectively induced global m^{6}A depletion in our non-model primary cells, its potential to introduce indirect effects necessitates cautious interpretation of the splicing responses.

Statistical analysis

All scripts used for computational analysis were written in Perl (http://www.perl.org), Python (http://www.python.org), or R (http://www.r-project.org). The Wilcoxon test, the χ^2 test, and the Student's *t*-test were performed using the wilcox.test, chisq.test, and t.test functions, respectively, in the R (version: 4.2.1) package.

Results and discussion

A moderate conservation of m^{6}A modification in mammals

We employed the ONT-DRS method (SQK-RNA002, Oxford Nanopore Technologies) to capture full-length transcripts and RNA methylation information from a collection of 142 tissue samples (liver, kidney, and brain) representing 21 species across 11 mammalian orders. This extensive sequencing effort resulted in a substantial dataset, comprising a staggering 39.90 terabytes of raw data. To refine the ONT-DRS data, we then generated 1731 GB of clean short-read transcriptome data (see the Materials and methods; Supplementary Figs S1–S3; Supplementary Tables S1–S4). By examining modification probability and overlapping ratio with MeRIP-seq data (see the Materials and methods), we implemented a modification probability of 0.90 to identity m^{6}A modification sites using m6Anet [65], which resulted in 786–24 011 highly confident m^{6}A sites, corresponding to 504–8511 genes (Fig. 1B; Supplementary Figs S4–S6; Supplementary Tables S5–S27). In each transcript, there are 1–17 m^{6}A sites present in the liver, 1–16 in the kidney, and 1–22 in the brain (Supplementary Fig. S7). The average numbers of m^{6}A modifications per transcript in the liver, kidney, and brain are 1.63, 1.76, and 2.11, respectively (Fig. 1C; Supplementary Fig. S8). This is consistent with findings from other studies, which report ∼1.7 peaks per gene in HepG2 cells [84]. The proportion of DRACH motifs (D = G/A/U, R = G/A, H = A/C/U) within a gene that are modified by m^{6}A (m^{6}A/DRACH) ranges from 4.05% to 12.84%, with a mean value of 7.86%. In contrast, the proportion of adenine residues modified by m^{6}A (m^{6}A/A) ranges from 0.26% to 0.87%, with an average of 0.52% (Fig. 1D). The general modification levels of tissues are relatively high in species such as ferrets and guinea pigs, while lower modification levels are observed in species such as mice, rats, pigs, and bats (Fig. 1B; Supplementary Fig. S4). To independently assess the global m^{6}A levels inferred from Nanopore sequencing across species, we additionally performed a bulk colorimetric immunoassay on 13 species. The global m^{6}A levels measured by the colorimetric assay showed a significant positive correlation with the transcriptome-wide modification estimates obtained from Nanopore sequencing (Spearman $\rho = 0.6$, $P = 0.03$; Pearson $r = 0.6$, $P = 0.03$) (Supplementary Table S28; Supplementary Figs S9 and S10). While absolute m^{6}A levels inferred from algorithmic site calling were generally higher than those obtained from antibody-based bulk measurements, reflecting inherent methodological differences, the strong concordance in rank order supports the comparative reliability of our cross-species m^{6}A abundance estimates.

PGLS [85] regression analyses further revealed a significant negative correlation between the m^{6}A ratio and both the cDNA genome size (liver: adjusted $R^2 = 0.52$, $P = 1.93 \times 10^{-2}$) and gene number (liver: adjusted $R^2 = 0.63$, $P = 3.39 \times 10^{-3}$) (Fig. 1E, F; Supplementary Fig. S11). Among the 15 414 orthologous genes analyzed, 25.54, 34.24, and 35.70% of them exhibited conserved m^{6}A modifications in liver, kidney, and brain tissues, respectively (Fig. 1G). Further-

more, when integrating a stoichiometric constraint to require quantitative consistency (Δ S < 0.473; Supplementary Fig. S12), the proportions of strictly conserved genes satisfying both positional and quantitative criteria were refined to 15.11, 22.62, and 23.89%, respectively (Supplementary Fig. S13). This is consistent with a previous study reporting that m^{6}A is present in ~30–40% of mRNA transcripts in vertebrates [86]. In addition, genes with highly conserved m^{6}A modification mainly revolved around the cell endomembrane system, receptor activities, and polysaccharide binding (Supplementary Fig. S14). At the sub-transcript level, evolutionary conservation was observed in the CDSs (44.29%), 3′-UTR (38.18%), and 5′-UTR (6.06%) across more than half of the species analyzed (Fig. 1H; Supplementary Fig. S15). However, at the single-nucleotide level, ~88 246 orthologous m^{6}A sites were identified among 5 639 266 adenine residues, yielding a conservation rate of only 1.56%. Overall, these findings indicate a moderate degree of evolutionary conservation of m^{6}A modifications across mammals, highlighting a diversity of these modifications at broader regulatory levels.

We then inferred the evolutionary origins of mammalian genes harboring m^{6}A modifications using phylostratigraphy analysis (Fig. 2A; Supplementary Table S29). Our results revealed a progressive decrease in the number of homologs to m^{6}A-modified genes across the early phylostrata (PS1 Eukaryota to PS8 Prototheria), followed by a resurgence in both the number and fixation rate of m^{6}A-modified genes in PS9 (Placentalia) (Fig. 2B–E). m^{6}A modification levels of ancient homologs increased from PS1 to PS5 (Eukaryota to Actinopteri), experienced a marked reduction at PS6 (Amphibia), and then recovered in Amniotes (PS7–PS9), forming an "evolutionary N-shaped curve" that was consistent across liver, kidney, and brain tissues (Fig. 2F–H). While this distinct pattern is consistent with a hypothesis of adaptive epigenetic remodeling during the amphibian-to-amniote transition, the apparent reduction in m^{6}A at PS6 should be interpreted with caution. Alternative explanations may contribute to the observed signal, including lineage–specific genomic features, compositional biases affecting motif availability, or differences in transcript architecture that influence m^{6}A site detectability. In addition, amphibian reference genomes are generally less complete and less well annotated than those of amniotes, which may lead to reduced sensitivity in ortholog identification, transcript boundary definition, or modification calling. Notably, although evolutionarily "new" m^{6}A homologs (PS6–PS9) were fewer than "old" m^{6}A homologs (PS1–PS5), they displayed significantly higher m^{6}A modification levels, indicating enhanced regulatory efficiency in recently evolved m^{6}A-modified homologs (Fig. 2B–E; Supplementary Fig. S16).

Selection signatures of m^{6}A modifications

Of the 21 examined mammals, orthologous genes exhibited a significantly higher proportion of m^{6}A methylation (the fraction of genes with m^{6}A modifications among all genes in a species) compared with species-specific genes (Fig. 3A, B; Supplementary Fig. S17; Supplementary Table S30). We sought to investigate the selection signatures associated with orthologous groups containing m^{6}A-modified sites. First, we applied "site models" [87, 88] to examine selection signals at specific sites where m^{6}A modifications occur. This analysis revealed that 4492 (48.42%) m^{6}A-modified sites exhibited signatures of positive selection, a proportion significantly higher than expected ($\chi^2 = 6.69$, $P = 9.6 \times 10^{-3}$) (Fig. 3C; see the Materials and methods). Next, we employed the "branch-site model" [88] to assess whether m^{6}A-modified sites experienced selective pressure along specific evolutionary lineages. For each ortholog, species with m^{6}A modifications were designated as foreground branches. Our results showed that 6.68% of m^{6}A-modified sites were under positive selection, which was slightly lower than the 7.23% observed in their non-m^{6}A-modified counterpart (Fig. 3D; Supplementary Figs S18 and S19). These findings suggest that codons harboring m^{6}A modifications are subject to positive selection; however, the specific residues commonly modified by m^{6}A are not consistently under selection in the shared species.

We also employed the FUBAR (fast, unconstrained Bayesian approximation) [89] model to evaluate the selection pressures and modification levels associated with m^{6}A sites. This analysis revealed that m^{6}A-modified sites exhibited significantly higher modification levels under negative selection compared with positive selection. Furthermore, a greater proportion of m^{6}A-modified sites demonstrated high credibility (posterior probability > 0.9) under negative selection than under positive selection. In contrast, non-m^{6}A-modified sites showed a higher representation of high credibility under positive selection pressures (i.e. $\alpha < \beta$, posterior probability > 0.9). On the other hand, m^{6}A-modified sites consistently displayed higher credibility under negative selection (i.e. $\alpha > \beta$, posterior probability > 0.9). Consistent with conservation score estimates (Fig. 3E–H), these findings indicate that most residues with m^{6}A modifications are conserved across phylogeny and constrained by negative selection.

To determine whether this evolutionary constraint extends beyond coding regions, we evaluated nucleotide-level conservation (phastCons) in the 3′-UTR. We found that m^{6}A sites within the 3′-UTR are significantly more conserved than closely matched, unmodified control adenines (Supplementary Fig. S20). Furthermore, to rule out the possibility that the elevated conservation observed at CDS m^{6}A sites is merely an artifact of underlying coding-related constraints, we performed two complementary control analyses. First, when strictly matching control adenines by codon position, CDS m^{6}A sites remained significantly more conserved across all three positions (Supplementary Fig. S21). Second, we restricted our analysis exclusively to 4D sites, where nucleotide substitutions are synonymous and do not alter the encoded amino acid. Even within this amino-acid-neutral background, CDS m^{6}A sites retained significantly higher conservation than matched non-m^{6}A controls (Supplementary Fig. S22). Together, these results demonstrate that m^{6}A-associated positions across both the CDS and 3′-UTR are subject to elevated, modification-specific evolutionary constraints that are independent of baseline amino acid identity or codon position biases.

Motif preferences and tissue-specific m^{6}A in mammals

Across the examined tissues (liver, kidney, and brain) in the analyzed species, the m^{6}A consensus motif DRACH (D = G/A/U, R = G/A, H = A/C/U) exhibited prominent enrichment. Among these, the GGACU motif was the most prevalent (Fig. 3I; Supplementary Fig. S23), followed by AGACU and GGACA (Fig. 3J; Supplementary Tables S31 and S32). In all three tissues, GGACU, GGACA, and AGACU were consistently the most enriched motifs (Supplementary Figs S24 and

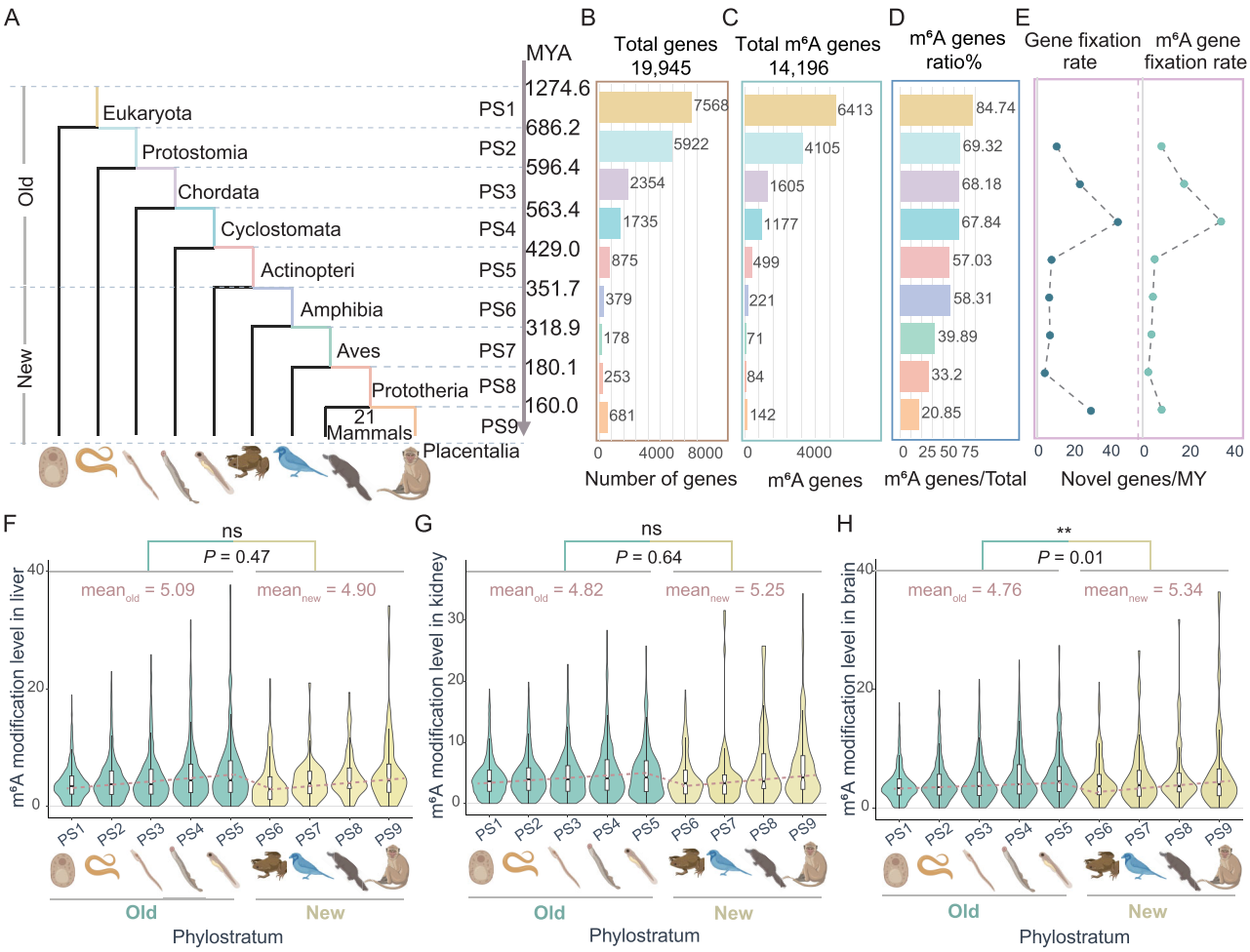

Figure 2. Enhanced regulatory efficacy of recently evolved m^{6}A-modified genes in the vertebrate brain. (**A**) Phylogenetic framework spanning nine phylostrata (PS1–PS9), with representative species [e.g. *Saccharomyces cerevisiae* (PS1), *Ornithorhynchus anatinus* (PS8)] and divergence times (MYA) from TimeTree. (**B** and **C**) Total genes (B) and m^{6}A-modified genes (C) per phylostratum, showing progressive reduction from PS1 (7568 genes; 6413 m^{6}A genes) to PS9 (681 genes; 142 m^{6}A genes). (**D**) m^{6}A gene ratio (%) per layer, declining from 84.74% (PS1) to 20.85% (PS9). (**E**) Gene fixation rates (novel genes/MY) and m^{6}A gene fixation rates, highlighting peaks at PS4 and PS9. (**F–H**) Tissue-specific m^{6}A modification levels (liver, kidney, and brain) comparing "old" (PS1–PS5) and "new" (PS6–PS9) genes. Brain tissue shows significantly higher m^{6}A levels in new genes (median 3.9 versus 3.6, $P = 0.01$).

S25). These findings align with previous studies on m^{6}A modifications in human cells using MeRIP-seq and CITS-m^{6}A-miCLIP, which similarly identified GGACU as the most enriched consensus motif [90, 91]. Furthermore, GGACU and GGACA exhibited the highest GERP scores and the lowest Rate4Site scores, suggesting that they are the most conserved among all m^{6}A motifs (Fig. 3K, L). The modification levels of motifs (M_{motif}) demonstrate both species- and tissue-specific patterns. GGACU consistently ranked as the most modified motif across all tissues and species, with AGACU generally ranking second (Supplementary Figs S26 and S27). This finding is further supported by a study employing m^{6}A-SAC-seq in human cells, which also confirmed GGACU as the most common motif and AGACU as the second most common [92].

Given that m^{6}A modification is regulated by a network of genes categorized as "writers", "readers", and "erasers", we examined whether tissue-level m^{6}A abundance covaries with the expression of these regulators across species while accounting for phylogenetic relatedness. In mammals, internal m^{6}A on mRNA is deposited primarily by the multiprotein METTL3–METTL14 writer complex together with auxiliary targeting factors (e.g. WTAP, VIRMA/KIAA1429, RBM15/15B, and ZC3H13), and is canonically decoded by YTH-domain proteins (YTHDF1/2/3 and YTHDC1/2) [93]; additional proteins (including IGF2BPs) have been proposed as context-dependent m^{6}A-associated readers. We found that the expression levels of most individual m^{6}A regulators were not significantly correlated with global m^{6}A modification levels (Supplementary Figs S28 and S29; Supplementary Table S33). However, a few genes exhibited correlations in specific tissues. For instance, the expression of *METTL16* (a "writer", adjusted $R^2 = 0.37$, $P = 0.01$, PGLS regression), *YTHDF2* (a "reader", adjusted $R^2 = 0.50$, $P = 7.00 \times 10^{-3}$, PGLS regression), and *IGF2BP3* (a "reader", adjusted $R^2 = 0.48$, $P = 1.30 \times 10^{-2}$, PGLS regression) showed significant correlations with global m^{6}A modification levels in the kidney (Fig. 3M). Notably, *METTL16* is a distinct m^{6}A methyltransferase reported to modify a comparatively restricted set of structured RNA substrates, with MAT2A being the best-characterized protein-coding target [94]. Similarly, YTHDF2, a critical reader protein, binds specifically to m^{6}A-modified RNAs, influencing their stability and degradation [95]. The

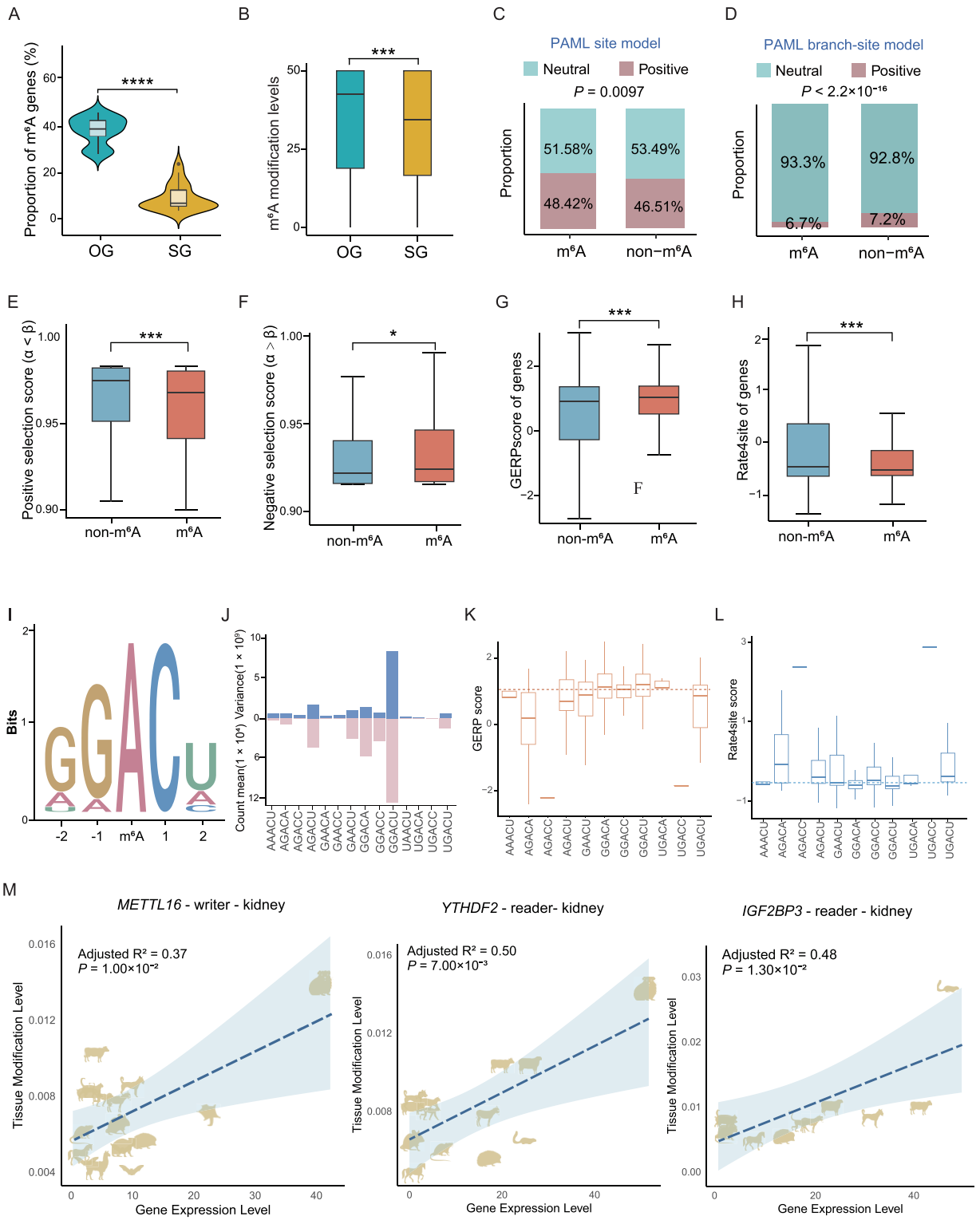

Figure 3. Species-specific patterns, motif preferences, and evolutionary selection of m^{6}A modifications. (**A** and **B**) Comparative analysis of m^{6}A modifications in orthogroup genes (OGs) versus species-specific genes (SGs). (**C** and **D**) Proportion and evolutionary analyses of m^{6}A versus non-m^{6}A sites under selection pressure. (**E** and **F**) Comparative selection analyses for m^{6}A modifications and adjacent non-m^{6}A sites. (**G** and **H**) Conservation scores (via GERP++ and Rate4Site) of m^{6}A-modified and non-modified sites. (**I**) Illustration of common m^{6}A motif patterns using a representative species (monkey) as an example. The GGACU motif is the most frequently observed across nearly all species. Detailed motif patterns for other species are provided in the supplementary figures. (**J**) Mean abundance and variability of m^{6}A motifs across mammalian species. Pink bars represent the mean counts of each motif across all samples, while blue bars represent the variance in motif counts across samples. (**K** and **L**) Tissue-specific conservation scores (GERP++ and Rate4Site) for each m^{6}A motif. These distributions highlight the evolutionary conservation of m^{6}A motifs across brain, kidney, and liver tissues. (**M**) Association of *METTL16* (writer), *YTHDF2*, and *IGF2BP3* (readers) expression with global m^{6}A levels in kidney tissue. Correlation analysis reveals significant positive relationships (PGLS, $P < 0.05$; dashed lines indicate 95% confidence intervals), suggesting that these genes act as tissue-specific drivers of m^{6}A deposition and recognition. Axes: normalized gene expression (CPM) versus m^{6}A modification level (M_{tissue}).

observed tissue specificity may reflect indirect coupling to methyl-donor metabolism (e.g. the METTL16–MAT2A axis) [96], differences in cellular composition, or tissue-specific regulatory programs. Nonetheless, because global m^{6}A is an aggregate phenotype influenced by multiple factors (e.g. writer complex stoichiometry, substrate transcriptome composition, methyl donor metabolism, and cellular composition), these associations should be interpreted as hypothesis-generating observations rather than direct evidence of causality.

We then adopted the widely recognized tau tissue specificity index [77] to evaluate the tissue-specific nature of m^{6}A methylation across various species (see the Materials and methods for details). tau ranges from 0 to 1, where 0 indicates widespread methylation and 1 indicates specificity. Our analysis revealed that llama, hyrax, guniea pig, and bats displayed relatively higher levels of tissue-specific m^{6}A methylation, whereas mouse, sheep, monkey, and dog presented with lower levels of tissue-specific methylation (Fig. 4A). To further investigate these findings, we ranked genes with tau values to examine the genomic positions of genes with high tissue-specific methylation (tau ranking top 100) and those with shared m^{6}A sites across species (tau ranking bottom 100). In species such as guniea pig and bats, the tissue-specific m^{6}A sites were predominantly located in the CDS (Supplementary Fig. S30). Conversely, in species such as monkey and mouse, the tissue-specific m^{6}A sites were more enriched in the 3′-UTR (Fig. 4B; Supplementary Tables S5–S25). These findings indicate that the functions of m^{6}A sites potentially vary depending on their positional context within mRNA and may be specific to particular species. In species with high modification levels, tissue-specific m^{6}A sites are mostly distributed in the CDS region, while in species with lower modification levels, m^{6}A sites shared by tissues are more often distributed in the 3′-UTR. We also found that species with lower m^{6}A methylation levels tend to a lower concentration of m^{6}A sites within the CDS, whereas those are more likely to have m^{6}A sites near the stop codon (encompassing both the 3′-UTR and CDS) (Fig. 4C; Supplementary Fig. S31). Additionally, we detected significant variations in m^{6}A methylation levels across tissues, notably with the brain and liver invariably presenting the highest and lowest methylation levels, respectively (Fig. 4D). This contrasted with gene expression patterns, where the majority of genes showed expression across all three tissues, and only a minor fraction exhibited tissue-specific expression (Fig. 4E; Supplementary Figs S32–S34).

The influence of m^{6}A modifications on RNA splicing

Previous research suggested that m^{6}A methylation can impact mRNA splicing; for instance, the loss of m^{6}A methylation leads to a decrease in alternative splicing complexity in *Drosophila* [97]. However, other studies also suggest that knocking down *METTL3* and *WTAP* to reduce m^{6}A methylation results in increased alternative splicing [11]. We then sought to explore the relationships between RNA splicing and modifications across mammals by employing splicing entropy to measure the complexity of alternative splicing. Interestingly, we observed a significant negative correlation between m^{6}A modification levels and alternative splicing complexity. Specifically, m^{6}A modification levels were significantly negatively correlated with splicing complexity in the liver (PGLS: $P = 0.03$), kidney (PGLS: $P = 0.40 \times 10^{-2}$), and brain (PGLS: $P = 0.01$) (Fig. 5A–D; Supplementary Table S34). Further experiments showed that cells treated with 3-DAA, a broad-spectrum inhibitor of m^{6}A methylation, exhibited a significant increase in alternative splicing complexity (PGLS: $P = 0.02$, $R = -0.72$), providing additional support for the observed relationship (Fig. 5E, F).

The observed correlation between global m^{6}A methylation levels and splicing complexity across species is particularly intriguing, as the relationship between these two biological processes remains elusive, even within the context of a single tissue or species. For example, YTHDC1, an m^{6}A-specific RNA-binding protein, can influence the activity of splicing factors such as SRSF, where Serine and Arginine-rich (SR) proteins function as splicing enhancers to increase splicing complexity [98]. In contrast, alternative findings suggest that splicing-associated EJC components have been reported to restrict m^{6}A deposition near splice junctions, potentially through local steric hindrance after or during spliceosome-mediated mRNA processing [99]. We then compared the m^{6}A distribution features within the 50 nt regions upstream of splice junctions across seven alternative splicing event types. The results revealed a striking enrichment of 8864 high-confidence m^{6}A sites near splice junctions in intron retention (RI) events, which lack EJC binding. In contrast, EJC-dependent splicing events (SE, AL, AF, A5, A3, and MX) exhibited significantly reduced m^{6}A deposition in homologous regions, with site counts of 253, 1513, 1737, 138, 867, and 1879, respectively (Supplementary Fig. S35). Further resolution of this spatial association through meta-event mapping revealed localized depletion of m^{6}A at distinct splice boundaries. Specifically, A5 events showed depletion at both the 5′ and 3′ boundaries of the event body, whereas A3 events displayed depletion restricted to the 5′ boundary, consistent with differences in the variable or fixed positioning of the upstream donor site (Supplementary Fig. S36). Quantitative analyses further demonstrated that actively spliced events are associated with reduced m^{6}A ratios within the immediate 25 nucleotide upstream window when compared with locally shifted background regions. This localized reduction progressively diminished when broader windows were examined and was not evident in RI events (Supplementary Fig. S37). In addition, alternative last exons exhibited a higher proportion of m^{6}A-positive exons relative to other splicing categories, linking m^{6}A spatial distribution to alternative terminal exon usage (Supplementary Fig. S38). This spatial distribution is consistent with a splice-junction-associated spatial constraint model, in which EJC components deposited during or after splicing may reduce local accessibility of m^{6}A methyltransferases near exon–exon junctions through steric hindrance. For RI events, which retain intronic sequence and therefore do not form canonical exon–exon junctions, the reduced opportunity for EJC deposition may decrease local junction-proximal constraint and potentially increase methyltransferase accessibility, which is consistent with the higher m^{6}A enrichment observed in RI-associated regions. Conversely, in splicing types with persistent EJC binding (e.g. SE/MX), m^{6}A deposition efficiency is markedly impaired. This is consistent with recent studies reporting splice-junction-proximal suppression, which propose that EJC deposition after splicing can limit methylation accessibility at nearby sites [99]. Notably, these studies also indicate that a substantial fraction of m^{6}A deposition occurs post-splicing. Overall, the observations are compatible with an EJC-associated spatial constraint model,

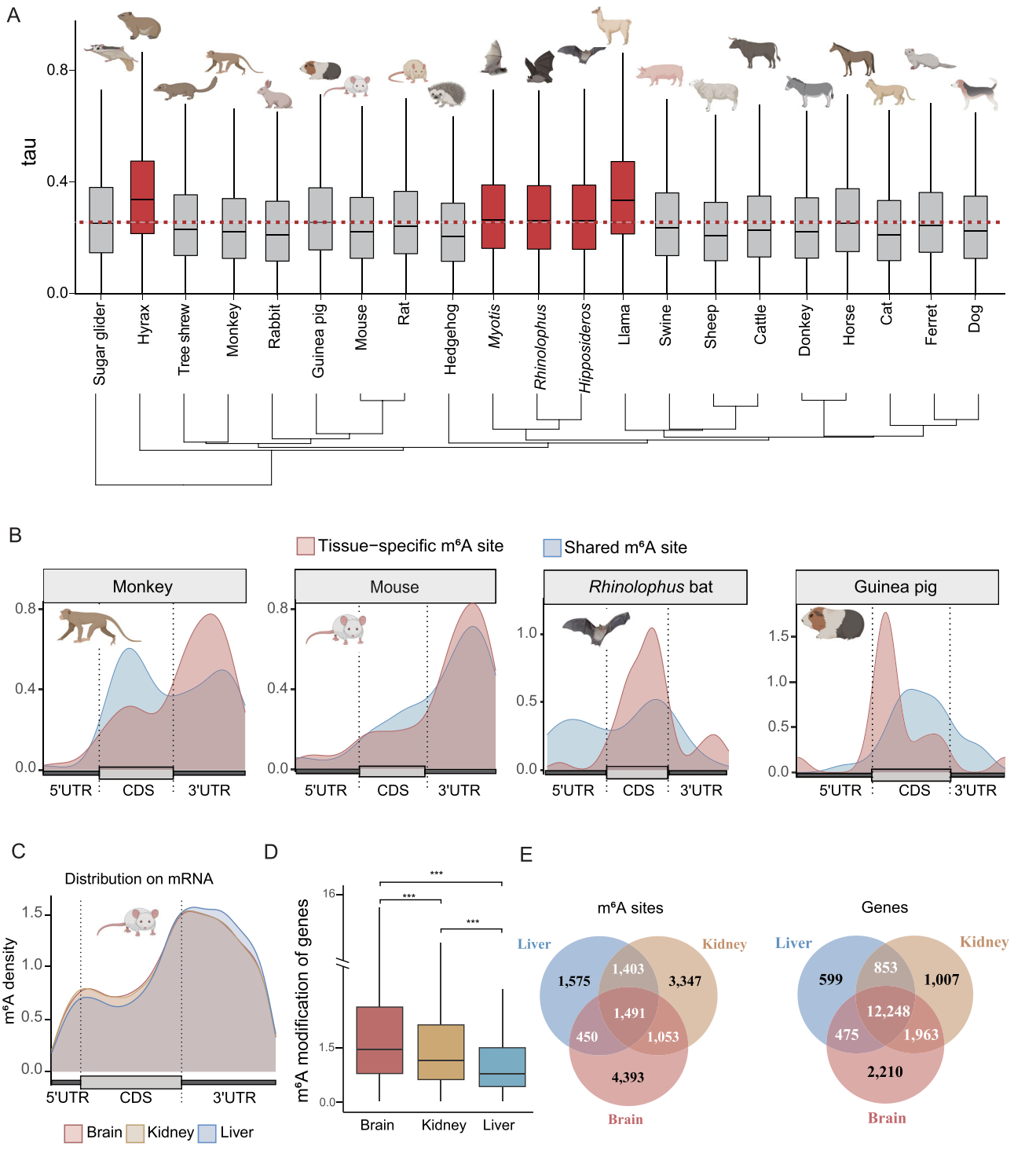

Figure 4. Distribution patterns and expression signatures of tissue-specific m^{6}A modification sites. (**A**) Tissue-specific m^{6}A modification levels across species. The red dashed line indicates the mean tissue specificity index (tau), which quantifies how distinctly m^{6}A modifications are distributed across tissues. The modification level of a tissue is calculated using the M_{tissue}, which represents the proportion of m^{6}A-modified reads to the total reads of DRACH motif sites within the tissue. (**B**) Comparison of mRNA distribution between tissue-specific m^{6}A sites and shared m^{6}A sites across all tissues. Tissue-specific m^{6}A sites, represented by the red curve, are contrasted with shared m^{6}A modification sites, represented by the blue curve, based on tau values. (**C**) Distribution of m^{6}A modification sites in different regions of mRNA in mouse brain, kidney, and liver. m^{6}A sites are predominantly clustered near the stop codon, encompassing both the CDS and the 3′-UTR. (**D**) Gene-level m^{6}A modification levels across the liver, kidney, and brain. The *y*-axis indicates the gene modification level for each tissue. (**E**) Identification of common and unique m^{6}A modification sites and their corresponding genes across the liver, kidney, and brain in mouse. This Venn diagram highlights overlaps and differences in m^{6}A-modified genes among the tissues.

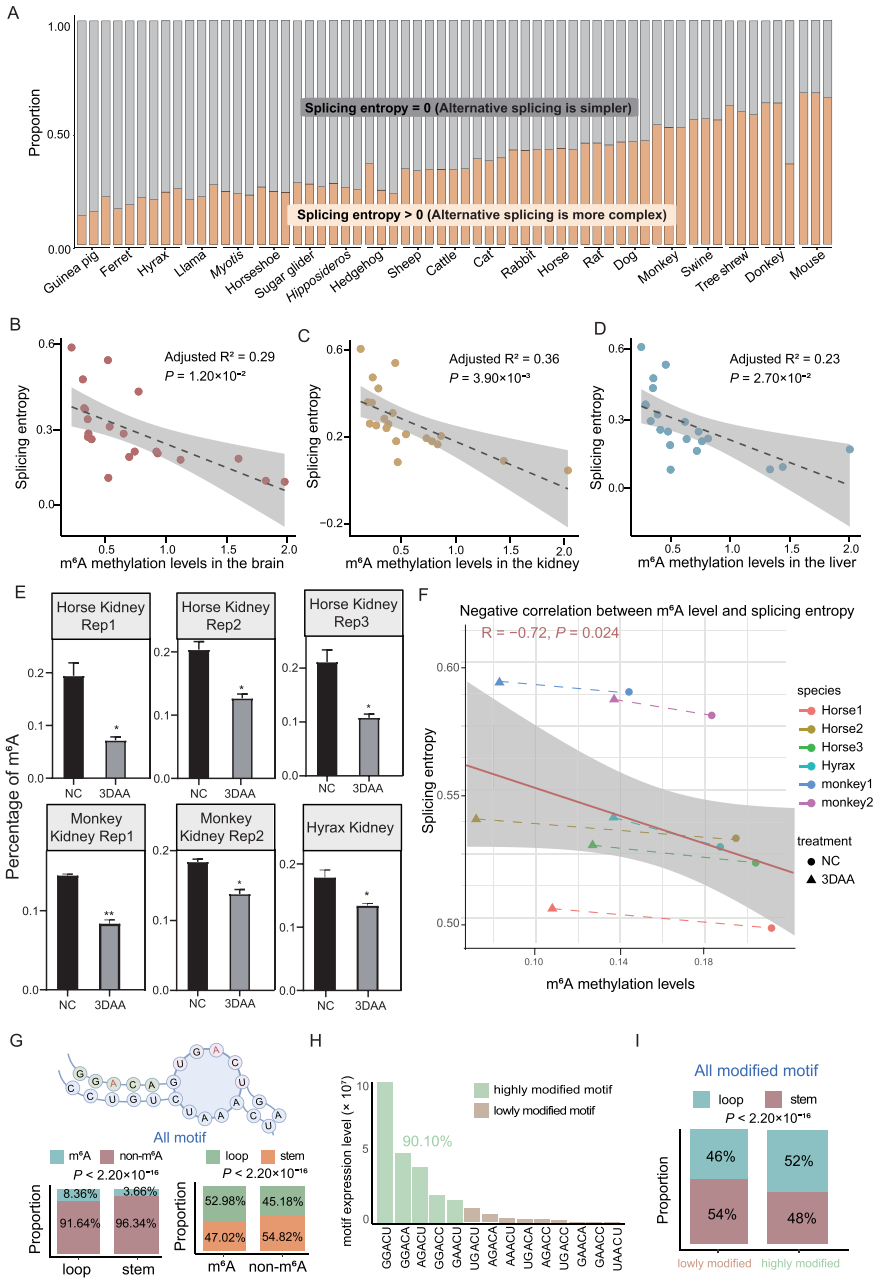

Figure 5. ^{6}A levels were significantly negatively correlated with splicing complexity. (**A**) Alternative splicing complexity across tissues and species quantified using splicing entropy (Shannon entropy). For each splicing event, entropy was calculated from the relative usage of alternative splicing pathways/isoforms; events with entropy = 0 were classified as simple (single pathway; gray), whereas events with entropy > 0 were classified as complex (multiple pathways with heterogeneous usage; orange). Each species is represented by three bars (liver, kidney, and brain from left to right). (**B–D**) Negative association between tissue m^{6}A modification levels and alternative splicing complexity across species in brain, kidney, and liver. The *y*-axis indicates the proportion of complex events (entropy > 0) in each tissue/species, and the *x*-axis indicates the tissue m^{6}A modification level. PGLS was used to account for phylogenetic non-independence. Note: here, "splicing complexity" refers to entropy-based isoform/pathway diversity within an event, rather than the frequency of specific alternative splicing event types (e.g. exon skipping or intron retention). (**E**) Quantification using the EpiQuik m^{6}A RNA Methylation Kit revealed that 100 μM 3-DAA treatment for 48 h significantly decreased the percentage of m^{6}A (Percentage of mA) in horse kidney, monkey kidney, and hyrax kidney cells compared with the negative control (NC). Data from three independent replicates (Reps 1–3). (**F**) For each sample, the NC and the 3DAA-treated group are connected by lines. The data demonstrate that following 3DAA treatment, all samples exhibit a reduction in m^{6}A levels accompanied by a significant increase in alternative splicing complexity; overall, m^{6}A modification levels are significantly negatively correlated with splicing complexity ($P = 0.024$, $R = -0.72$). (**G**) Correlation between RNA secondary structure and m^{6}A methylation. The upper panel illustrates the distribution of m^{6}A modification sites on RNA secondary structures, with red adenine residues denoting m^{6}A-modified sites. Motifs located in loops are highlighted by pink background circles, and those in stems are highlighted by light green circles. The lower panel presents a contingency table showing the proportions of m^{6}A-modified nucleotide sites located in loops versus stems. (**H**) Modification rates and rank variations among different m^{6}A motifs. The five motifs with the highest modification rates—GGACU, GGACC, GGACA, GAACU, and AGACU—are grouped as the "high-modification" group, while all other motifs are grouped as the "low-modification" group. Light green bars represent the expression levels of highly modified motifs, while brownish-pink bars represent the expression levels of motifs modified to a low extent. Together, the top five motifs account for 90.10% of the total expression. (**I**) Structural distribution of high- and low-modification motifs. A higher proportion of adenine sites in high-modification motifs are located in loops compared with stems, while a higher proportion of adenine sites in low-modification motifs are located in stems.

while not precluding contributions from co-transcriptional regulatory mechanisms.

In parallel, m^{6}A modifications are also known to modulate the secondary structure of mRNA and lncRNA, altering their interactions with heterogeneous nuclear RNA-binding proteins (hnRNPs) and ultimately leading to the inhibition of alternative splicing [2, 100]. Given that SRSF proteins can be attracted to RNA loop regions to enhance splicing [101, 102], and that hnRNPs can block alternative splicing upon binding to these loops [103], it is plausible that the intricacies of alternative splicing are tied to the secondary structure of RNA. Interestingly, our analyses reveal that m^{6}A modification sites are significantly more frequent in RNA loop regions than in stems (Fig. 5G; Supplementary Table S35). Furthermore, heavily modified motifs (comprising 90.10% of all motif occurrences) are also enriched in loops (Fig. 5H, I), suggesting that SR proteins and hnRNPs may exert opposing regulatory roles in this context, influenced by m^{6}A modifications. Despite these insights, the precise mechanisms underlying this relationship remain unclear and warrant further investigation.

Cross-species correlation between life history traits and m^{6}A modification

The dense sampling of mammalian species enabled us to investigate whether genes harboring m^{6}A modifications are associated with life history traits across the phylogeny. To address this, we conducted a regression analysis under a phylogenetic framework (the BM model versus the OU model; see the Materials and methods) to identify genes whose m^{6}A modification level correlates with life history data (i.e. longevity, adult body weight, and basal metabolic rate) (see the Materiasls and methods and Supplementary Table S36). Our analysis identified that 250, 164, and 379 genes show significant correlation with longevity, adult body weight, and basal metabolic rate, respectively, for m^{6}A (Fig. 6A–F; Supplementary Fig. S39; Supplementary Table S37). Among these, five genes (*MLF1*, *CPLANE2*, *PMF1*, *RWDD4*, and *PLLP*) demonstrated a significant association with m^{6}A modification across the three life history traits. Notably, *MLF1*, *RWDD4*, and *PLLP* exhibit m^{6}A modifications at orthologous sites across a broad range of species, with *MLF1* having 17 sites, *RWDD4* having 11 sites, and *PLLP* having 3 sites, all shared by > 10 species (Fig. 6G; Supplementary Fig. S40). It is reported that *MLF1* plays a multifaceted role in regulating the cell cycle, apoptosis, and histone modifications, and it is critical for tissue homeostasis and development. Intriguingly, *MLF1* has also been identified as a pro-aging epigenetic factor, as it recruits EP300 to facilitate the opening of condensed chromatin, thus activating senescence-associated effectors [104]. *RWDD4*, on the other hand, influences cell proliferation, migration, and invasion, and acts as a regulatory factor in cancers such as bladder cancer and glioma [105, 106]. While the functional consequence of m^{6}A of those genes is currently unknown, these findings underscore the potential regulatory roles of m^{6}A modifications in mediating the biological processes underpinning *MLF1* and *RWDD4*, as well as their involvement in development, metabolism, and aging.

To further explore the relationship between life history traits and m^{6}A modification, we used longevity as a representative measure, examining selective pressures and m^{6}A modification levels across mammals. The 21 mammalian species were categorized into two groups: long-lived (n = 7) and short-lived (n = 14) (Supplementary Table S36), based on a cut-off of 26 years [107]. To assess the selective pressure on genes, we calculated the selection strength parameter k using the RELAX [71] tool from the HYPHY package, where $k > 1$ indicates intensified selection, while a value < 1 suggests relaxed selection. Using k to quantify selection pressures, genes associated with longevity were categorized into four groups (Fig. 7A, B). In long-lived mammals, the number of genes with low levels of m^{6}A modification is similar under relaxed and intensified selection. However, genes with higher levels of m^{6}A modification in long-lived species are more frequently subject to relaxed selection than intensified selection (Supplementary Fig. S41). Furthermore, the proportion of genes with m^{6}A modifications under either relaxed or intensified selection is notably higher in long-lived species, with percentages reaching 58.47% in the liver, 64.71% in the kidney, and 61.28% in the brain (Fig. 7C, D).

It if interesting to have found that, across tissues, eight genes (*SGK1*, *PLA2G15*, *IL6R*, *OSMR*, *ADGRA3*, *N4BP1*, *NDN*, and *FAM220A*) show higher modification levels and intensified selection in long-lived species compared with short-lived ones (Fig. 7E–I; Supplementary Fig. S42). While specific details on m^{6}A modification of these genes are limited, some of them have the potential to interact with the aging process. For example, *METTL3* directly catalyzes m^{6}A methylation on serum/glucocorticoid regulated kinase 1 (SGK1) mRNA [108], a gene involved in regulating reproductive senescence and life span. The m^{6}A reader YTHDF2 can specifically target interleukin-6 receptor (IL-6R) mRNA by recognizing the m^{6}A-modified site, decreasing the stability of IL-6R mRNA [109], which plays a significant role in the aging process and age-related diseases. These observations suggest that both genetic factors and m^{6}A modifications impose constraints on these genes, shaping their roles in aging and longevity regulation.

Conclusions

This study provides an initial and informative survey of the m^{6}A modification landscape across 21 non-model mammals, revealing intricate patterns and showcasing its evolutionary stability. An important discovery from our investigation is that ~32% of m^{6}A-modified genes are conserved across species, and m^{6}A modification sites exhibit stronger purifying selection compared with non-modified sites, underscoring their functional significance. Furthermore, we found that the splicing entropy shows a significant correlation with m^{6}A methylation. Notably, in long-lived species, genes with higher levels of m^{6}A modification are more frequently subject to relaxed selection than intensified selection. Overall, this research enriches our comprehension of m^{6}A modification across the mammalian lineage, clarifying its pivotal roles in gene regulation and its potential to influence life history traits.

Nonetheless, several technical limitations inherent to Nanopore DRS should be considered in the context of the present study [110]. The accuracy of computational identification algorithms, such as m6Anet, is intrinsically influenced by the composition of their training datasets and by the sequencing chemistries applied, including protocol transitions (e.g. RNA002 to RNA004). Although current models exhibit strong cross-species generalizability and effectively suppress background signals when assessed using modification-free IVT RNA, site-level quantification may remain sensitive

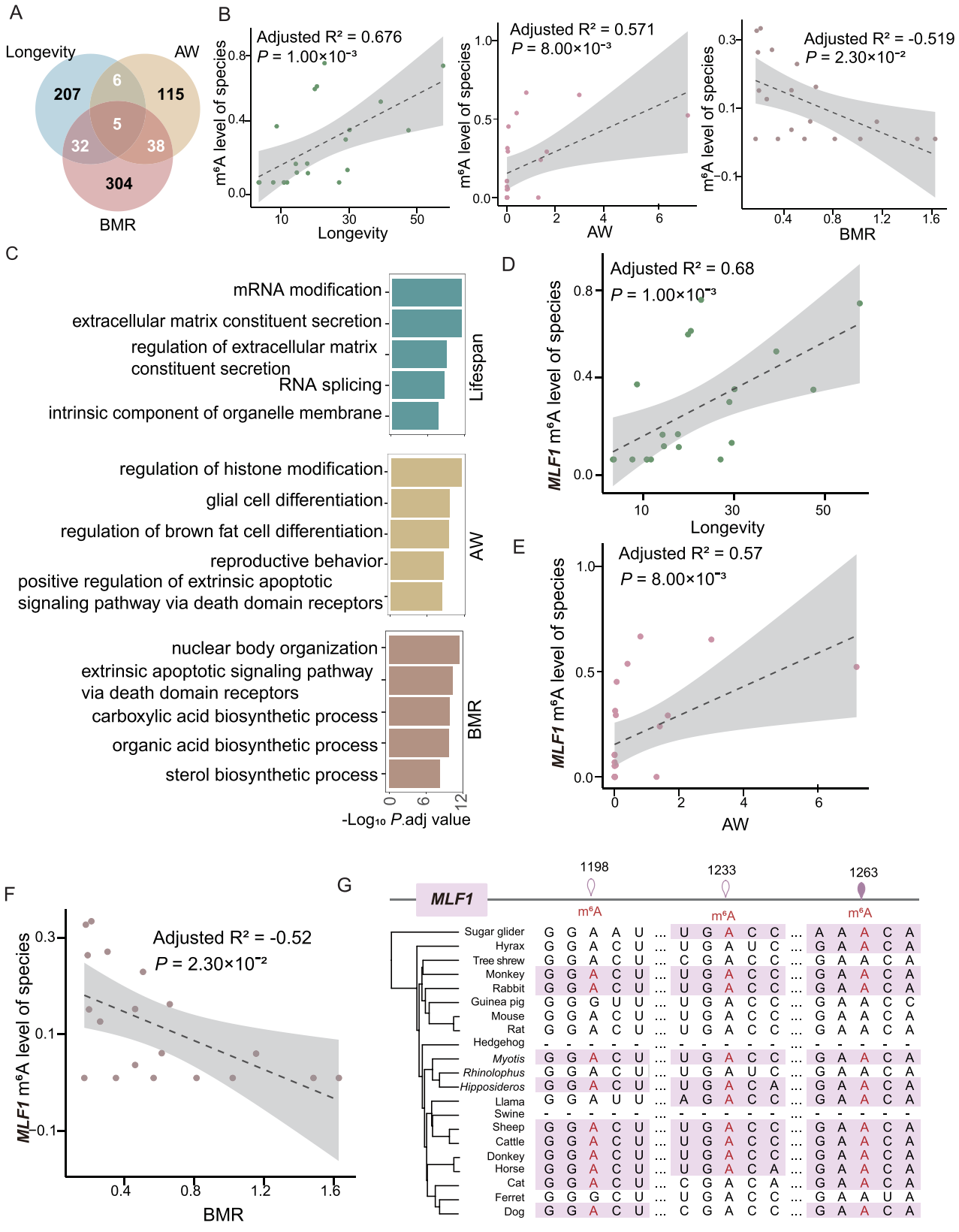

Figure 6. Evolutionary relationships between life history traits and m^{6}A modification across 21 mammalian species. (**A**) Number of genes whose m^{6}A modification levels are significantly correlated with longevity, maximum body weight, and basal metabolic rate. (**B**) Correlation between m^{6}A modification levels of the *MLF1* gene and the three life history traits (PGLS). (**C**) Pathway enrichment analysis via polysel for genes positively correlated with m^{6}A modification, life span, maximum adult weight (AW), and basal metabolic rate (BMR). Significance levels are shown as $-\log_{10} P_{adj}$ value. (**D–F**) *MLF1* was significantly associated with all three life history traits and m^{6}A modification levels. (**G**) Alignment and m^{6}A modification sites in *MLF1*. Conserved modification sites are marked in the alignment, with the red 'A' representing m^{6}A-modified sites and the pink background denoting the motif sequence modified by m^{6}A. Key m^{6}A-modified positions (e.g. 1198, 1233, and 1263) are highlighted, with position 1263 conserved across orthologous sites in 13 species.

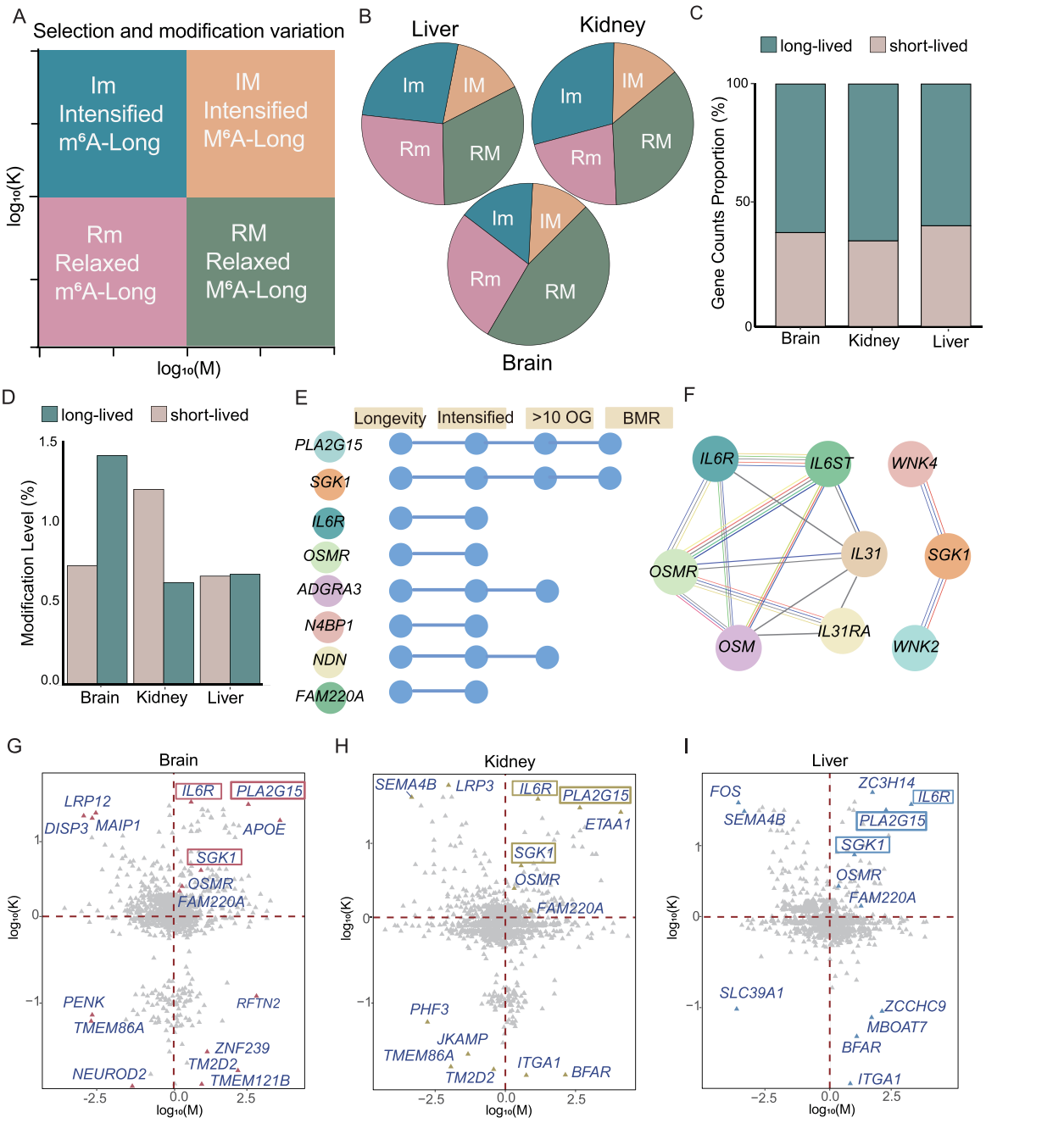

Figure 7. Evolutionary relationships between m^{6}A modification and selective pressures across 21 mammalian species. (**A**) Classification of genes based on m^{6}A modification levels and selection pressures in long-lived ($n = 7$, ≥ 26 years) and short-lived species ($n = 14$, < 26 years). Genes were categorized into: (i) genes with higher levels of m^{6}A modification that undergo intensified selection in long-lived species compared with short-lived species (IM); (ii) genes with higher levels of m^{6}A modification but experiencing relaxed selection in long-lived species compared with short-lived species (RM); (iii) genes with lower levels of m^{6}A modification that undergo intensified selection in long-lived species compared with short-lived species (Im); and (iv) genes with lower levels of m^{6}A modification but experiencing relaxed selection in long-lived species compared with short-lived species (Rm). Selection pressure was determined by the parameter k, with $k > 1$ indicating intensified selection and $k < 1$ indicating relaxed selection. (**B**) Tissue-specific proportions of genes across the four selection-modification classifications (IM, RM, Im, and Rm) in the liver, kidney, and brain. RM genes comprise 32.2, 35.3, and 45.9% of the liver, kidney, and brain, respectively, followed by Rm, IM, and Im genes. (**C** and **D**) Comparative statistics of genes with m^{6}A modifications in long-lived and short-lived species. The left bar chart shows a higher proportion of genes with m^{6}A modifications under selection in long-lived species (58.47%, liver; 64.71%, kidney; 61.28%, brain). The right bar chart compares the m^{6}A modification levels (measured as the number of reads at m^{6}A sites/reads at DRACH sites) in the liver, kidney, and brain of long- and short-lived species. In the liver, the modification level was 0.6865% in long-lived species and 0.6966% in short-lived species; in the kidney, it was 1.2316% in long-lived species and 0.6446% in short-lived species; and in the brain, it was 0.7515% in long-lived species and 1.4442% in short-lived species. (**E** and **F**) Functional and evolutionary insights into genes with higher m^{6}A modification levels and intensified selection in long-lived species. The table highlights examples of these genes, including genes conserved across > 10 orthologous species (">10 OG") and genes whose m^{6}A levels are associated with the basal metabolic rate (BMR). Functional enrichment analysis reveals links to processes such as interleukin signaling and inflammatory response. (**G–I**) Distribution of tissue-specific genes (brain, kidney, and liver) with elevated m^{6}A modifications and selection pressures in long-lived species, classified following criteria from (D). Genes identified in (G) are highlighted with rectangles to indicate functional significance.

to statistical variability, particularly under conditions of limited read depth or very low true modification stoichiometry. In addition, the identification of modification sites necessarily involves a balance between precision and recall. Accordingly, although our comparative analyses were restricted to high-confidence sites supported by at least 20 reads and a site-level modification probability exceeding 0.9, this conservative criterion may lead to an underestimation of the overall prevalence of functionally relevant m^{6}A sites that occur at lower modification levels within the transcriptome.

Acknowledgements

The authors are grateful to the editors and the anonymous reviewers for their valuable suggestions and comments, which have led to the improvement of this article. We thank Jing Yang, Jiwei Qi, and Pengcheng Wang for supporting sample collection and preparation. The authors declare no competing interests.

Author contributions: Xuming Zhou and Xiaoxiao Zhang conceived the study and designed the project, with input from M.L. who provided some ideas; Xiaoxiao Zhang, Weiqiang Liu, W.C., and Z.Z. performed the sample collection and preparation, G.L., M.L., and Z.L. provided assistance; Xiaoxiao Zhang conducted data curation, bioinformatics analysis, visualization, and wrote the manuscript; Y.D. and Wenfu Liu performed experiments; Xuming Zhou and Xiaoxiao Zhang designed figures; Xuming Zhou acquired funding and supervised the study; Xuming Zhou, Xiaoxiao Zhang, Z.Z., Weiqiang Liu, G.L., X.L., and C.H. provided suggestions for data analysis; Xuming Zhou and Xiaoxiao Zhang revised the manuscript. All authors contributed to data interpretation.

Supplementary data

Supplementary data are available at NAR online.

Conflict of interest

The authors declare no competing interests.

Funding

The National Natural Science Foundation of China [32270437]; National Key Research and Development Projects of the Ministry of Science and Technology of China [2023YFC3304000]; the Institute of Zoology, Chinese Academy of Sciences [2023IOZ0104]; and the Prevention and Control of Emerging and Major Infectious Diseases-National Science and Technology Major Project [2026ZD01911000].

Data availability

All data are available in the main text or the supplementary data. Materials and reagents described in this study are either commercially available or available on request from the corresponding author. The Oxford Nanopore DRS sequencing data and NGS data are deposited in the Genome Sequence Archive in the National Genomics Data Center, China National Center for Bioinformation/Beijing Institute of Genomics, Chinese Academy of Sciences (accession no. GSA: CRA015510 for all species) that are publicly accessible at https://ngdc.cncb.ac.cn/gsa.

The original code has been deposited at https://github.com/XiaoxiaoZhang57/Evolutionary-analysis-of-m6A-in-mammals.git and Zenodo at https://doi.org/10.5281/zenodo.20085328.

Any additional information required to reanalyze the data reported in this paper is available from the lead contact upon request.

References

1. Boccaletto P, Stefaniak F, Ray A *et al.* MODOMICS: a database of RNA modification pathways. 2021 update. *Nucleic Acids Res* 2022;50:D231–5. https://doi.org/10.1093/nar/gkab1083
2. Busch A, Hertel KJ. Evolution of SR protein and hnRNP splicing regulatory factors. *WIREs RNA* 2012;3:1–12. https://doi.org/10.1002/wrna.100
3. Cantara WA, Crain PF, Rozenski J *et al.* The RNA modification database, RNAMDB: 2011 update. *Nucleic Acids Res* 2010;39:D195–201. https://doi.org/10.1093/nar/gkq1028
4. Wei C-M, Gershowitz A, Moss B. Methylated nucleotides block 5′ terminus of HeLa cell messenger RNA. *Cell* 1975;4:379–86. https://doi.org/10.1016/0092-8674(75)90158-0
5. Wei W, Ji X, Guo X *et al.* Regulatory role of N^6-methyladenosine (m^{6}A) methylation in RNA processing and human diseases. *J Cell Biochem* 2017;118:2534–43. https://doi.org/10.1002/jcb.25967
6. Desrosiers R, Friderici K, Rottman F. Identification of methylated nucleosides in messenger RNA from Novikoff hepatoma cells. *Proc Natl Acad Sci USA* 1974;71:3971–5. https://doi.org/10.1073/pnas.71.10.3971
7. Alarcón CR, Lee H, Goodarzi H *et al.* N^6-methyladenosine marks primary microRNAs for processing. *Nature* 2015;519:482–5.
8. Patil DP, Chen C-K, Pickering BF *et al.* m^{6}A RNA methylation promotes XIST-mediated transcriptional repression. *Nature* 2016;537:369–73. https://doi.org/10.1038/nature19342
9. Schwartz S. m^{1}A within cytoplasmic mRNAs at single nucleotide resolution: a reconciled transcriptome-wide map. *RNA* 2018;24:1427–36. https://doi.org/10.1261/rna.067348.118
10. Georgeson J, Schwartz S. No evidence for ac^{4}C within human mRNA upon data reassessment. *Mol Cell* 2024;84:1601–10. https://doi.org/10.1016/j.molcel.2024.03.017
11. Ping X-L, Sun B-F, Wang L *et al.* Mammalian WTAP is a regulatory subunit of the RNA N^6-methyladenosine methyltransferase. *Cell Res* 2014;24:177–89. https://doi.org/10.1038/cr.2014.3
12. Liu N, Dai Q, Zheng G *et al.* N^6-methyladenosine-dependent RNA structural switches regulate RNA–protein interactions. *Nature* 2015;518:560–4. https://doi.org/10.1038/nature14234
13. Shi H, Wei J, He C. Where, when, and how: context-dependent functions of RNA methylation writers, readers, and erasers. *Mol Cell* 2019;74:640–50. https://doi.org/10.1016/j.molcel.2019.04.025
14. Yen Y-P, Chen J-A. The m^{6}A epitranscriptome on neural development and degeneration. *J Biomed Sci* 2021;28:40–51. https://doi.org/10.1186/s12929-021-00734-6
15. Destefanis E, Avşar G, Groza P *et al.* A mark of disease: how mRNA modifications shape genetic and acquired pathologies. *RNA* 2021;27:367–89. https://doi.org/10.1261/rna.077271.120
16. Barbieri I, Kouzarides T. Role of RNA modifications in cancer. *Nat Rev Cancer* 2020;20:303–22. https://doi.org/10.1038/s41568-020-0253-2
17. Haruehanroengra P, Zheng YY, Zhou Y *et al.* RNA modifications and cancer. *RNA Biol* 2020;17:1560–75. https://doi.org/10.1080/15476286.2020.1722449
18. Berulava T, Buchholz E, Elerdashvili V *et al.* Changes in m^{6}A RNA methylation contribute to heart failure progression by modulating translation. *Eur J Heart Fail* 2020;22:54–66. https://doi.org/10.1002/ejhf.1672

19. Liu T, Wei Q, Jin J *et al.* The m^{6}A reader YTHDF1 promotes ovarian cancer progression via augmenting EIF3C translation. *Nucleic Acids Res* 2020;48:3816–31. https://doi.org/10.1093/nar/gkaa048
20. Zhao BS, Roundtree IA, He C. Post-transcriptional gene regulation by mRNA modifications. *Nat Rev Mol Cell Biol* 2017;18:31–42. https://doi.org/10.1038/nrm.2016.132
21. Yang Y, Hsu PJ, Chen Y-S *et al.* Dynamic transcriptomic m^{6}A decoration: writers, erasers, readers and functions in RNA metabolism. *Cell Res* 2018;28:616–24. https://doi.org/10.1038/s41422-018-0040-8
22. Shen L, Liang Z, Wong CE *et al.* Messenger RNA modifications in plants. *Trends Plant Sci* 2019;24:328–41. https://doi.org/10.1016/j.tplants.2019.01.005
23. Xiang Y, Laurent B, Hsu C-H *et al.* RNA m^{6}A methylation regulates the ultraviolet-induced DNA damage response. *Nature* 2017;543:573–6. https://doi.org/10.1038/nature21671
24. Winkler R, Gillis E, Lasman L *et al.* m^{6}A modification controls the innate immune response to infection by targeting type I interferons. *Nat Immunol* 2019;20:173–82. https://doi.org/10.1038/s41590-018-0275-z
25. Engel M, Eggert C, Kaplick PM *et al.* The role of m^{6}A/m-RNA methylation in stress response regulation. *Neuron* 2018;99:389–403.e9. https://doi.org/10.1016/j.neuron.2018.07.009
26. Zhou J, Wan J, Gao X *et al.* Dynamic m^{6}A mRNA methylation directs translational control of heat shock response. *Nature* 2015;526:591–4. https://doi.org/10.1038/nature15377
27. Wang X, Zhao BS, Roundtree IA *et al.* N^6-methyladenosine modulates messenger RNA translation efficiency. *Cell* 2015;161:1388–99. https://doi.org/10.1016/j.cell.2015.05.014
28. Esteve-Puig R, Bueno-Costa A, Esteller M. Writers, readers and erasers of RNA modifications in cancer. *Cancer Lett* 2020;474:127–37. https://doi.org/10.1016/j.canlet.2020.01.021
29. Xiong X, Hou L, Park YP *et al.* Genetic drivers of m6A methylation in human brain, lung, heart and muscle. *Nat Genet* 2021;53:1156–65. https://doi.org/10.1038/s41588-021-00890-3
30. Shafik AM, Zhang F, Guo Z *et al.* N^6-methyladenosine dynamics in neurodevelopment and aging, and its potential role in Alzheimer's disease. *Genome Biol* 2021;22:17–36. https://doi.org/10.1186/s13059-020-02249-z
31. Zhang X, Yin H, Zhang X *et al.* N^6-methyladenosine modification governs liver glycogenesis by stabilizing the glycogen synthase 2 mRNA. *Nat Commun* 2022;13:7038. https://doi.org/10.1038/s41467-022-34808-2
32. Ma L, Zhao B, Chen K *et al.* Evolution of transcript modification by N^6-methyladenosine in primates. *Genome Res* 2017;27:385–92. https://doi.org/10.1101/gr.212563.116
33. Meyer KD, Saletore Y, Zumbo P *et al.* Comprehensive analysis of mRNA methylation reveals enrichment in 3′ UTRs and near stop codons. *Cell* 2012;149:1635–46. https://doi.org/10.1016/j.cell.2012.05.003
34. Peer E, Rechavi G, Dominissini D. Epitranscriptomics: regulation of mRNA metabolism through modifications. *Curr Opin Chem Biol* 2017;41:93–8. https://doi.org/10.1016/j.cbpa.2017.10.008
35. Trixl L, Lusser A. The dynamic RNA modification 5-methylcytosine and its emerging role as an epitranscriptomic mark. *WIREs RNA* 2019;10:e1510. https://doi.org/10.1002/wrna.1510
36. Perešíni P, Boža V, Brejová B *et al.* Nanopore base calling on the edge. *Bioinformatics* 2021;37:4661–7. https://doi.org/10.1093/bioinformatics/btab528
37. De Coster W, D'hert S, Schultz DT *et al.* NanoPack: visualizing and processing long-read sequencing data. *Bioinformatics* 2018;34:2666–9. https://doi.org/10.1093/bioinformatics/bty149
38. Wang JR, Holt J, McMillan L *et al.* FMLRC: hybrid long read error correction using an FM-index. *BMC Bioinformatics* 2018;19:50–61. https://doi.org/10.1186/s12859-018-2051-3
39. Li H. Minimap2: pairwise alignment for nucleotide sequences. *Bioinformatics* 2018;34:3094–100. https://doi.org/10.1093/bioinformatics/bty191
40. Danecek P, Bonfield JK, Liddle J *et al.* Twelve years of SAMtools and BCFtools. *GigaScience* 2021;10:giab008. https://doi.org/10.1093/gigascience/giab008
41. Pertea M, Pertea GM, Antonescu CM *et al.* StringTie enables improved reconstruction of a transcriptome from RNA-seq reads. *Nat Biotechnol* 2015;33:290–5. https://doi.org/10.1038/nbt.3122
42. Pertea G, Pertea M. GFF utilities: gffRead and GffCompare. *F1000Res* 2020;9:304. https://doi.org/10.12688/f1000research.23297.1
43. Renshaw MA, Olds BP, Jerde CL *et al.* The room temperature preservation of filtered environmental DNA samples and assimilation into a phenol–chloroform–isoamyl alcohol DNA extraction. *Mol Ecol Resour* 2015;15:168–76. https://doi.org/10.1111/1755-0998.12281
44. Servant N, Varoquaux N, Lajoie BR *et al.* HiC-Pro: an optimized and flexible pipeline for Hi-C data processing. *Genome Biol* 2015;16:259–70. https://doi.org/10.1186/s13059-015-0831-x
45. Weisenfeld NI, Kumar V, Shah P *et al.* Direct determination of diploid genome sequences. *Genome Res* 2017;27:757–67. https://doi.org/10.1101/gr.214874.116
46. Luo R, Liu B, Xie Y *et al.* SOAPdenovo2: an empirically improved memory-efficient short-read de novo assembler. *GigaScience* 2012;1:18. https://doi.org/10.1186/2047-217X-1-18
47. Roach MJ, Schmidt SA, Borneman AR. Purge Haplotigs: allelic contig reassignment for third-gen diploid genome assemblies. *BMC Bioinformatics* 2018;19:1–10. https://doi.org/10.1186/s12859-018-2485-7
48. Durand NC, Shamim MS, Machol I *et al.* Juicer provides a one-click system for analyzing loop-resolution Hi-C experiments. *Cell Syst* 2016;3:95–8. https://doi.org/10.1016/j.cels.2016.07.002
49. Dudchenko O, Batra SS, Omer AD *et al.* De novo assembly of the *Aedes aegypti* genome using Hi-C yields chromosome-length scaffolds. *Science* 2017;356:92–5. https://doi.org/10.1126/science.aal3327
50. Durand NC, Robinson JT, Shamim MS *et al.* Juicebox provides a visualization system for Hi-C contact maps with unlimited zoom. *Cell Syst* 2016;3:99–101. https://doi.org/10.1016/j.cels.2015.07.012
51. Chen N. Using RepeatMasker to identify repetitive elements in genomic sequences. *Curr Protoc Bioinformatics* 2004;Chapter 4:Unit4.10. https://doi.org/10.1002/0471250953.bi0410s05
52. Abrusán G, Grundmann N, DeMester L *et al.* TEclass—a tool for automated classification of unknown eukaryotic transposable elements. *Bioinformatics* 2009;25:1329–30. https://doi.org/10.1093/bioinformatics/btp084
53. Tarailo-Graovac M, Chen N. Using RepeatMasker to identify repetitive elements in genomic sequences. *Curr Protoc Bioinformatics* 2009;Chapter 4:4.10.1–4.10.14. https://doi.org/10.1002/0471250953.bi0410s25
54. Benson G. Tandem repeats finder: a program to analyze DNA sequences. *Nucleic Acids Res* 1999;27:573–80. https://doi.org/10.1093/nar/27.2.573
55. Stanke M, Diekhans M, Baertsch R *et al.* Using native and syntenically mapped cDNA alignments to improve de novo gene finding. *Bioinformatics* 2008;24:637–44. https://doi.org/10.1093/bioinformatics/btn013
56. Burge C, Karlin S. Prediction of complete gene structures in human genomic DNA. *J Mol Biol* 1997;268:78–94. https://doi.org/10.1006/jmbi.1997.0951
57. Kent WJ. BLAT—the BLAST-like alignment tool. *Genome Res* 2002;12:656–64. https://doi.org/10.1101/gr.229202

58. Birney E, Clamp M, Durbin R. GeneWise and genomewise. *Genome Res* 2004;14:988–95. https://doi.org/10.1101/gr.1865504
59. Haas BJ, Papanicolaou A, Yassour M *et al.* De novo transcript sequence reconstruction from RNA-seq using the Trinity platform for reference generation and analysis. *Nat Protoc* 2013;8:1494–512. https://doi.org/10.1038/nprot.2013.084
60. Lowe TM, Eddy SR. tRNAscan-SE: a program for improved detection of transfer RNA genes in genomic sequence. *Nucleic Acids Res* 1997;25:955–64. https://doi.org/10.1093/nar/25.5.955
61. Nawrocki EP, Kolbe DL, Eddy SR. Infernal 1.0: inference of RNA alignments. *Bioinformatics* 2009;25:1335–7. https://doi.org/10.1093/bioinformatics/btp157
62. Griffiths-Jones S, Bateman A, Marshall M *et al.* Rfam: an RNA family database. *Nucleic Acids Res* 2003;31:439–41. https://doi.org/10.1093/nar/gkg006
63. Revell LJ. phytools 2.0: an updated R package for phylogenetic comparative biology (and other things). *PeerJ* 2012;12:e16505. https://doi.org.10.7717/peerj.16505
64. Loman NJ, Quick J, Simpson JT. A complete bacterial genome assembled de novo using only nanopore sequencing data. *Nat Methods* 2015;12:733–5. https://doi.org/10.1038/nmeth.3444
65. Hendra C, Pratanwanich PN, Wan YK *et al.* Detection of m6A from direct RNA sequencing using a multiple instance learning framework. *Nat Methods* 2022;19:1590–8. https://doi.org/10.1038/s41592-022-01666-1
66. Emms DM, Kelly S. OrthoFinder: phylogenetic orthology inference for comparative genomics. *Genome Biol* 2019;20:238–52. https://doi.org/10.1186/s13059-019-1832-y
67. Buchfink B, Xie C, Huson DH. Fast and sensitive protein alignment using DIAMOND. *Nat Methods* 2015;12:59–60. https://doi.org/10.1038/nmeth.3176
68. Katoh K, Standley DM. MAFFT multiple sequence alignment software version 7: improvements in performance and usability. *Mol Biol Evol* 2013;30:772–80. https://doi.org/10.1093/molbev/mst010
69. Castresana J. Selection of conserved blocks from multiple alignments for their use in phylogenetic analysis. *Mol Biol Evol* 2000;17:540–52. https://doi.org/10.1093/oxfordjournals.molbev.a026334
70. Kumar S, Suleski M, Craig JM *et al.* TimeTree 5: an expanded resource for species divergence times. *Mol Biol Evol* 2022;39:msac174. https://doi.org/10.1093/molbev/msac174
71. Wertheim JO, Murrell B, Smith MD *et al.* RELAX: detecting relaxed selection in a phylogenetic framework. *Mol Biol Evol* 2014;32:820–32. https://doi.org/10.1093/molbev/msu400
72. Huber CD, Kim BY, Lohmueller KE. Population genetic models of GERP scores suggest pervasive turnover of constrained sites across mammalian evolution. *PLoS Genet* 2020;16:e1008827. https://doi.org/10.1371/journal.pgen.1008827
73. Pupko T, Bell RE, Mayrose I *et al.* Rate4Site: an algorithmic tool for the identification of functional regions in proteins by surface mapping of evolutionary determinants within their homologues. *Bioinformatics* 2002;18:S71–7. https://doi.org/10.1093/bioinformatics/18.suppl_1.S71
74. Domazet-Lošo T, Brajković J, Tautz D. A phylostratigraphy approach to uncover the genomic history of major adaptations in metazoan lineages. *Trends Genet* 2007;23:533–9. https://doi.org/10.1016/j.tig.2007.08.014
75. Kumar S, Stecher G, Suleski M *et al.* TimeTree: a resource for timelines, timetrees, and divergence times. *Mol Biol Evol* 2017;34:1812–9. https://doi.org/10.1093/molbev/msx116
76. Arendsee Z, Li J, Singh U *et al.* Phylostratr: a framework for phylostratigraphy. *Bioinformatics* 2019;35:3617–27. https://doi.org/10.1093/bioinformatics/btz171
77. Kryuchkova-Mostacci N, Robinson-Rechavi M. A benchmark of gene expression tissue-specificity metrics. *Briefings Bioinform* 2017;18:205–14. https://doi.org/10.1093/bib/bbw00
78. Trincado JL, Entizne JC, Hysenaj G *et al.* SUPPA2: fast, accurate, and uncertainty-aware differential splicing analysis across multiple conditions. *Genome Biol* 2018;19:1–11. https://doi.org/10.1186/s13059-018-1417-1
79. Hu Y, Huang Y, Du Y *et al.* DiffSplice: the genome-wide detection of differential splicing events with RNA-seq. *Nucleic Acids Res* 2013;41:e39–. https://doi.org/10.1093/nar/gks1026
80. Ritchie W, Granjeaud S, Puthier D *et al.* Entropy measures quantify global splicing disorders in cancer. *PLoS Comput Biol* 2008;4:e1000011. https://doi.org/10.1371/journal.pcbi.1000011
81. Orme D, Freckleton R, Thomas G *et al.* The caper package: comparative analysis of phylogenetics and evolution in R. *R package version* 2013;5(2):1–36.
82. Hofacker IL. Vienna RNA secondary structure server. *Nucleic Acids Res* 2003;31:3429–31. https://doi.org/10.1093/nar/gkg599
83. Cui X, Wei Z, Zhang L *et al.* Guitar: an R/Bioconductor package for gene annotation guided transcriptomic analysis of RNA-related genomic features. *Biomed Res Int* 2016;2016:1–8. https://doi.org/10.1155/2016/8367534 .
84. Dominissini D, Moshitch-Moshkovitz S, Schwartz S *et al.* Topology of the human and mouse m^{6}A RNA methylomes revealed by m6A-seq. *Nature* 2012;485:201–6. https://doi.org/10.1038/nature11112
85. Blomberg SP, Lefevre JG, Wells JA *et al.* Independent contrasts and PGLS regression estimators are equivalent. *Syst Biol* 2012;61:382–91. https://doi.org/10.1093/sysbio/syr118
86. Patil DP, Pickering BF, Jaffrey SR. Reading m^{6}A in the transcriptome: m^{6}A-binding proteins. *Trends Cell Biol* 2018;28:113–27. https://doi.org/10.1016/j.tcb.2017.10.001
87. Yang Z. PAML 4: phylogenetic analysis by maximum likelihood. *Mol Biol Evol* 2007;24:1586–91. https://doi.org/10.1093/molbev/msm088
88. Zhang J, Nielsen R, Yang Z. Evaluation of an improved branch-site likelihood method for detecting positive selection at the molecular level. *Mol Biol Evol* 2005;22:2472–9. https://doi.org/10.1093/molbev/msi237
89. Murrell B, Moola S, Mabona A *et al.* FUBAR: a Fast, Unconstrained Bayesian AppRoximation for inferring selection. *Mol Biol Evol* 2013;30:1196–205. https://doi.org/10.1093/molbev/mst030
90. Vu LP, Pickering BF, Cheng Y *et al.* The N6-methyladenosine (m6A)-forming enzyme METTL3 controls myeloid differentiation of normal hematopoietic and leukemia cells. *Nat Med* 2017;23:1369–76. https://doi.org/10.1038/nm.4416
91. Linder B, Grozhik AV, Olarerin-George AO *et al.* Single-nucleotide-resolution mapping of m6A and m6Am throughout the transcriptome. *Nat Methods* 2015;12:767–72. https://doi.org/10.1038/nmeth.3453
92. Hu L, Liu S, Peng Y *et al.* m^{6}A RNA modifications are measured at single-base resolution across the mammalian transcriptome. *Nat Biotechnol* 2022;40:1210–9. https://doi.org/10.1038/s41587-022-01243-z
93. Liao S, Sun H, Xu C. YTH domain: a family of N^6-methyladenosine (m^{6}A) readers. *Genomics Proteomics Bioinformatics* 2018;16:99–107. https://doi.org/10.1016/j.gpb.2018.04.002
94. Satterwhite ER, Mansfield KD. RNA methyltransferase METTL16: targets and function. *WIREs RNA* 2022;13:e1681. https://doi.org/10.1002/wrna.1681
95. Du H, Zhao Y, He J *et al.* YTHDF2 destabilizes m6A-containing RNA through direct recruitment of the CCR4–NOT deadenylase complex. *Nat Commun* 2016;7:12626. https://doi.org/10.1038/ncomms12626
96. Mendel M, Chen K-M, Homolka D *et al.* Methylation of structured RNA by the m^{6}A writer METTL16 is essential for mouse embryonic development. *Mol Cell* 2018;71:986–1000. https://doi.org/10.1016/j.molcel.2018.08.004
97. Haussmann IU, Bodi Z, Sanchez-Moran E *et al.* m^{6}A potentiates Sxl alternative pre-mRNA splicing for robust Drosophila sex

determination. *Nature* 2016;540:301–4. https://doi.org/10.1038/nature20577
98. Xiao W, Adhikari S, Dahal U *et al.* Nuclear m^{6}A reader YTHDC1 regulates mRNA splicing. *Mol Cell* 2016;61:507–19. https://doi.org/10.1016/j.molcel.2016.01.012
99. He PC, Wei J, Dou X *et al.* Exon architecture controls mRNA m^{6}A suppression and gene expression. *Science* 2023;379:677–82. https://doi.org/10.1126/science.abj9090
100. König J, Zarnack K, Rot G *et al.* iCLIP reveals the function of hnRNP particles in splicing at individual nucleotide resolution. *Nat Struct Mol Biol* 2010;17:909–15.
101. Li K, Wang Z. Splicing factor SRSF2-centric gene regulation. *Int J Biol Sci* 2021;17:1708–15. https://doi.org/10.7150/ijbs.58888
102. Li D, Yu W, Lai M. Towards understandings of serine/arginine-rich splicing factors. *Acta Pharm Sin B* 2023;13:3181–207. https://doi.org/10.1016/j.apsb.2023.05.022
103. Jobbins AM, Campagne S, Weinmeister R *et al.* Exon-independent recruitment of SRSF1 is mediated by U1 snRNP stem–loop 3. *EMBO J* 2022;41:e107640. https://doi.org/10.15252/embj.2021107640
104. Lv J, Chen Q, Wang J *et al.* Downregulation of MLF1 safeguards cardiomyocytes against senescence-associated chromatin opening. *Nucleic Acids Res* 2025;53:gkae1176. https://doi.org/10.1093/nar/gkae1176
105. Hou Y. MiR–506 inhibits cell proliferation, invasion, migration and epithelial–to-mesenchymal transition through targeting RWDD4 in human bladder cancer. *Oncol Lett* 2019;17:73–8. https://doi.org/10.3892/ol.2018.959
106. Zheng Y, Xie J, Xu X *et al.* LncRNA DDX11-AS1 exerts oncogenic roles in glioma through regulating miR-499b-5p/RWDD4 axis. *Onco Targets Ther* 2021;14:157–64. https://doi.org/10.2147/OTT.S278986
107. Jobson RW, Nabholz B, Galtier N. An evolutionary genome scan for longevity-related natural selection in mammals. *Mol Biol Evol* 2010;27:840–7. https://doi.org/10.1093/molbev/msp293
108. Huang J, Feng Q, Dong Z *et al.* METTL3 aggravates intimal hyperplasia by facilitating the m^{6}A–YTHDC1-dependent SGK1 gene transcription. *Arterioscler Thromb Vasc Biol* 2025; 45:e437–53. https://doi.org/10.1161/ATVBAHA.125.322961
109. Zeng Z, Lan Y, Zhang L *et al.* The m^{6}A reader YTHDF2 alleviates the inflammatory response by inhibiting IL-6R/JAK2/STAT1 pathway-mediated high-mobility group box-1 release. *Burns Trauma* 2023;11:tkad023. https://doi.org/10.1093/burnst/tkad023
110. Anreiter I, Mir Q, Simpson JT *et al.* New twists in detecting mRNA modification dynamics. *Trends Biotechnol* 2021;39:72–89. https://doi.org/10.1016/j.tibtech.2020.06.002

Received: November 8, 2025. **Revised:** March 29, 2026. **Accepted:** May 7, 2026